

Geochemistry, Geophysics, Geosystems®



RESEARCH ARTICLE

10.1029/2022GC010833

Key Points:

- One-year ocean-bottom geophysical investigation on the oldest Pacific provides seismic mantle structure of the region
- Detailed 3-D mantle structure implies complex evolution process of Pacific Plate
- Our model implies thermochemical modification of the upper mantle by plume interaction or small-scale convection

Supporting Information:

Supporting Information may be found in the online version of this article.

Correspondence to:

Y. Kim,
younghkim@snu.ac.kr

Citation:

Kang, H., Kim, Y., Hung, S.-H., Lin, P.-Y. P., Isse, T., Kawakatsu, H., et al. (2023). Seismic velocity structure of upper mantle beneath the oldest Pacific seafloor: Insights from finite-frequency tomography. *Geochemistry, Geophysics, Geosystems*, 24, e2022GC010833. <https://doi.org/10.1029/2022GC010833>

Received 14 DEC 2022

Accepted 18 JUL 2023

Author Contributions:

Conceptualization: YoungHee Kim

Data curation: Hyunsun Kang, YoungHee Kim, Takehi Isse, Hitoshi Kawakatsu, Hisashi Utada, Nozomu Takeuchi, Hajime Shiobara, Hiroko Sugioka, Seung-Sep Kim

Formal analysis: Hyunsun Kang, Takehi Isse

Funding acquisition: YoungHee Kim, Hitoshi Kawakatsu, Sang-Mook Lee, Hisashi Utada

© 2023 The Authors. *Geochemistry, Geophysics, Geosystems* published by Wiley Periodicals LLC on behalf of American Geophysical Union. This is an open access article under the terms of the [Creative Commons Attribution-NonCommercial License](#), which permits use, distribution and reproduction in any medium, provided the original work is properly cited and is not used for commercial purposes.

Seismic Velocity Structure of Upper Mantle Beneath the Oldest Pacific Seafloor: Insights From Finite-Frequency Tomography

Hyunsun Kang¹ , YoungHee Kim¹ , Shu-Huei Hung² , Pei-Ying Patty Lin³ , Takehi Isse⁴ , Hitoshi Kawakatsu^{4,5} , Sang-Mook Lee¹ , Hisashi Utada⁴ , Nozomu Takeuchi⁴ , Hajime Shiobara⁴ , Hiroko Sugioka⁶ , and Seung-Sep Kim⁷

¹School of Earth and Environmental Sciences, Seoul National University, Seoul, Republic of Korea, ²Department of Geosciences, National Taiwan University, Taipei, Taiwan, ³Department of Earth Sciences, National Taiwan Normal University, Taipei, Taiwan, ⁴Earthquake Research Institute, The University of Tokyo, Tokyo, Japan, ⁵Institute of Earth Sciences, Academia Sinica, Taipei, Taiwan, ⁶Department of Planetology, Graduate School of Science, Kobe University, Kobe, Japan, ⁷Department of Geological Sciences, Chungnam National University, Daejeon, Republic of Korea

Abstract The oldest oceanic basin (160–180 Ma) in the western Pacific is the birthplace of the Pacific Plate and is thus essential for understanding the formation and evolution of the oceanic plate. However, the upper mantle structure beneath the region has not been thoroughly investigated because of the remoteness and difficulties of long-term in situ seismic measurements at the ocean bottom. From 2018 to 2019, the Oldest-1 experiment on the oldest seafloor was conducted as part of the international Pacific Array initiative. We present the first three-dimensional *P*-wave velocity structure down to a depth of 350 km based on the relative travel time residuals of teleseismic earthquakes recorded by 11 broadband ocean-bottom seismometers operated during the Oldest-1 experiment. Our result shows a fast *P*-wave velocity anomaly (V_p perturbation of 2%–4% faster than average) at a depth of 95–185 km beneath the northeast of the study area. This structure is interpreted as evidence of dry, viscous, and rigid materials at depths below the lithosphere. Two slow anomalies (V_p perturbation of 2%–4% slower than average) are seen beneath the southwestern and eastern (the oldest seafloor >170 Ma) parts of the array site. The low-velocity zones are found at depths of 95–305 km. The observed velocity structures can be indicative of plume activities that affected the upper mantle as the Pacific Plate migrated over hotspots from the southeast. Alternatively, the observed velocity features may provide seismic evidence for small-scale sublithospheric convection.

1. Introduction

Plate tectonics is a fundamental framework for understanding the Earth's evolution. Understanding the onset of spreading is an integral part of this paradigm. Unfortunately, few areas exist where such a process can be directly observed. The oldest seafloor in the western Pacific (160–180 Ma) is a unique location to investigate the opening of the oceanic plate. Unlike the Atlantic and Indian Oceans, the oldest portion of the Pacific is not covered by thick sediments. This unique feature makes the oldest Pacific basin an ideal site for in-depth studies.

Despite its importance, direct seismic observations on the seafloor have been limited for logistical and technical reasons. However, recent advancements in broadband ocean bottom seismometer (BBOBS) technology (Barcheck et al., 2020; Barruol & Sigloch, 2013; Eilon, Gaherty, et al., 2022; Shiobara et al., 2021; Stähler et al., 2016; Sumy et al., 2015), together with long-term deployments, have made it possible to study the vast mantle regions covered by water, broadening our understanding of plate tectonics. These developments have enabled researchers to explore various aspects of plate tectonics, including the distribution of local seismicity in oceanic environments (Bie et al., 2020; Ito et al., 2023), seismic velocity structures (Isse et al., 2019; Lin et al., 2016; Takeo et al., 2013, 2016, 2018; Takeuchi et al., 2020) and intrinsic attenuation structure (Takeuchi et al., 2017) of the oceanic lithosphere-asthenosphere system, and seismic velocity structure of the oceanic Moho and boundaries associated with the oceanic crust and plate interface (Janiszewski & Abers, 2015).

The utilization of the BBOBS network has played a critical role in clarifying oceanic mantle plumes and seismic characteristics of the oceanic lithosphere (e.g., Ma et al., 2020; Russell et al., 2019; Schlömer et al., 2017; Tsekhmistrenko et al., 2021). One important method for analyzing BBOBS data is body-wave travel time

Investigation: Hyunsun Kang, YoungHee Kim, Takehi Isse, Hitoshi Kawakatsu, Hisashi Utada, Hajime Shiobara, Hiroko Sugioka, Seung-Sep Kim

Methodology: Pei-Ying Patty Lin, Hitoshi Kawakatsu

Project Administration: YoungHee Kim, Hitoshi Kawakatsu, Sang-Mook Lee, Hisashi Utada

Resources: YoungHee Kim

Software: Shu-Huei Hung

Supervision: YoungHee Kim

Validation: Hyunsun Kang, YoungHee Kim, Shu-Huei Hung, Pei-Ying Patty Lin, Hitoshi Kawakatsu

Visualization: Hyunsun Kang

Writing – original draft: Hyunsun Kang

Writing – review & editing: Hyunsun Kang, YoungHee Kim, Shu-Huei Hung, Pei-Ying Patty Lin, Takehi Isse, Hitoshi Kawakatsu, Sang-Mook Lee, Hisashi Utada, Nozomu Takeuchi, Hajime Shiobara, Hiroko Sugioka, Seung-Sep Kim

tomography to infer structures created by dynamic mantle processes. For instance, using such an approach around the Tristan da Cunha island, Schlömer et al. (2017) have found evidence for a conduit of the Tristan mantle plume, which may have played a role in the Mesozoic opening of the South Atlantic. In addition, the Réunion Hotspot and Upper Mantle-Réunions Unterer Mantle (RHUM-RUM) experiment showed a tree-like structure of the Indo-African mantle plume centered on Africa, the Indian Ocean, and the Southern Ocean, which appeared to rise to the surface from the core-mantle boundary (Tsekhmistrenko et al., 2021). As for the Pacific Ocean, several studies have recently focused on understanding the deep seismic structure of the Pacific upper mantle. For example, Isse et al. (2019) obtained isotropic and anisotropic upper-mantle *S*-wave velocity models of the Pacific Plate from surface-wave tomography using over 200 BBOBSs and land stations.

Since the early 2010s, several OBS array experiments have been conducted on the Pacific seafloor. One is the Normal Oceanic Mantle (NOMan) project (2010–2014), which deployed two arrays of BBOBSs and ocean-bottom electro-magnetometers (OBEMs) in two areas of 130 and 140 Myr-old seafloors in the north-western Pacific to investigate the lithosphere-asthenosphere system of the “normal” oceanic mantle. Despite the similar plate thermal ages below the two sites, significant differences in seismic velocity and electrical conductivity structures were observed at a depth of the asthenosphere and interpreted as a consequence of different asthenospheric dynamics, possibly sublithospheric small-scale convection (Baba et al., 2017; Takeo et al., 2018). The NoMelt was performed on the 70 Myr-old Pacific seafloor southeast of Hawaii, away from major tectonic structures, including intraplate volcanoes. This experiment provided a set of new constraints on seismic anisotropy and attenuation structures, as well as flow dynamics within the oceanic lithosphere-asthenosphere system (Lin et al., 2016; Ma et al., 2020; Russell et al., 2019). The Pacific ocean-bottom seismometer (OBS) Research into Convecting Asthenosphere (ORCA) experiment on the 40 Ma Pacific Plate, conducted during 2018–2020 as part of the Pacific Array initiative, provided tomographic evidence for small-scale convective rolls (Eilon, Zhang, et al., 2022). In the western Pacific, several OBS experiments have been conducted to elucidate the physical condition of the lithosphere-asthenosphere system, including the 2009–2010 Pacific Lithosphere Anisotropy and Thickness Experiment (PLATE) project (Shintaku et al., 2014; Takeo et al., 2014) and the 2014–2017 Ontong-Java Plateau (OJP) array experiment (Isse et al., 2021).

The Pacific Array is an international large-scale array initiative designed to cover a large portion of the Pacific basin with an array of arrays of ocean-bottom geophysical instruments (Kawakatsu & Utada, 2017; <http://eri-ndc.eri.u-tokyo.ac.jp/PacificArray/>). The initiative aims to provide constraints on Earth's structure and geodynamic evolution. As part of this effort, the Oldest-1 experiment was conducted on the oldest seafloor (160–180 Ma; Figure 1) to investigate the early evolution of the Pacific Plate.

The oldest part of the plate, known as the Pacific triangle, is located east of the Mariana Trench. Magnetic anomalies characterize the study area in three orientations (NW-SE trending Hawaiian lineation, NE-SW-trending Japanese lineation, and E-W trending Phoenix lineation; Figure 1) (Nakanishi et al., 1992). The triangular magnetic lineations suggest that the Pacific Plate was initially formed at a point location by seafloor spreading in three different directions associated with the Izanagi, Farallon, and Phoenix Plates (Müller et al., 2008). The paleo-spreading directions of the oldest Pacific Plate do not follow the current plate motion directions (Becker et al., 2014).

To gain a better understanding of the study area, it is crucial to examine its geological and geophysical features. The study area includes two oceanic basins: the Pigafetta Basin (PB) in the northeast and the East Mariana Basin (EMB) in the southwest, which are covered by Cretaceous flood basalts (Coffin et al., 2006). The Magellan Seamount Trail (MST) is located between the two basins (Abrams et al., 1993). The Earth's largest flood basalt province, the OJP, is situated south of the array site. The oldest section of the Pacific Plate sits on an unusually shallow seafloor with a thin elastic plate thickness (McNutt, 1998; McNutt & Fischer, 1987; Smith et al., 1989; Winterer et al., 1993; Wolfe & McNutt, 1991). Furthermore, the subsidence rate of this section of the Pacific Plate is slower than what is predicted by conductive heat loss models (Parsons & Sclater, 1977), and this region is thus considered as an ancient superswell.

This study presents a three-dimensional (3-D) *P*-wave model of the oldest Pacific basin from the BBOBS data acquired from the Oldest-1 experiment. The experiment, which involved two seagoing cruises, enabled a detailed investigation of the deep mantle structure of the oldest Pacific for the first time. Our tomography model successfully images the structure at depths of 95–350 km below the oldest seafloor and further provides new insights into the evolution process of the Pacific Plate.

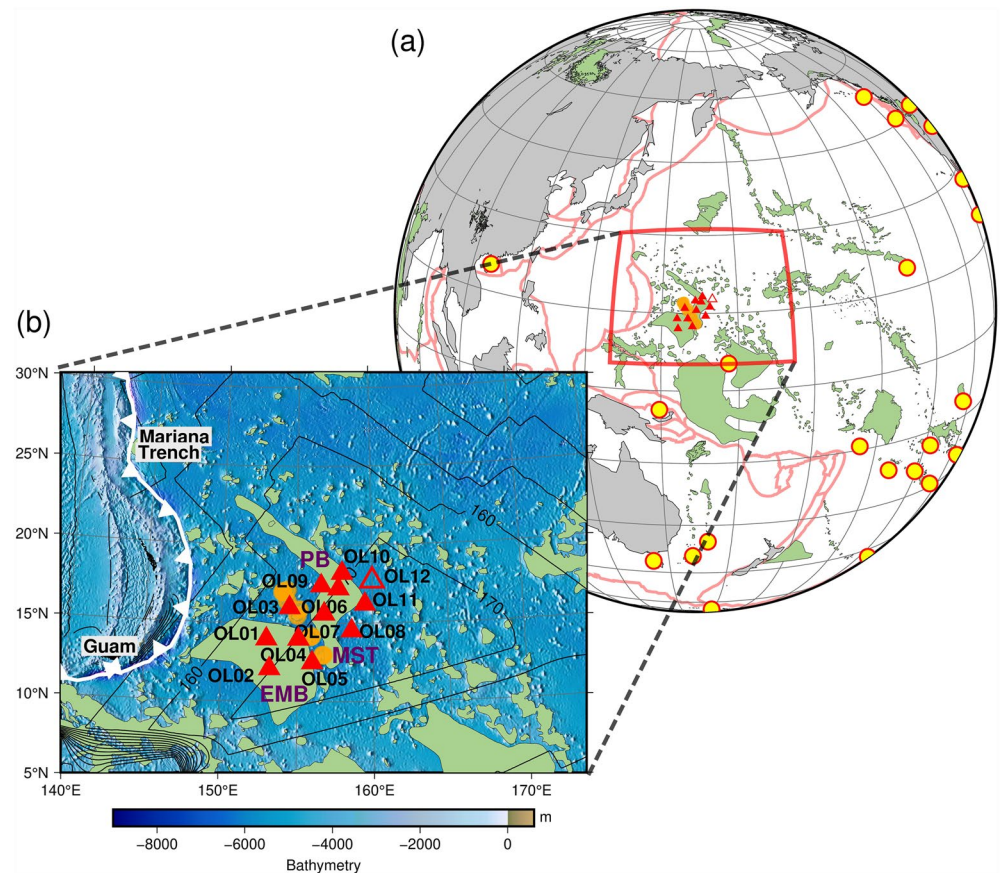


Figure 1. Maps showing the distribution of broadband ocean bottom seismometers (BBOBSs) of the Oldest-1 array. (a) Red triangles show the locations of 11 BBOBSs that provided three-component seismograms and DPG records, while an open triangle indicates a station that recorded DPG data only. Plate boundaries from Bird (2003) are shown as pink lines. The global distribution of large igneous provinces is shown as green-colored areas (Coffin et al., 2006). Yellow circles with red outlines indicate the distribution of hotspots (Jackson et al., 2021). The red box shows the boundaries of the zoomed-in map of the western Pacific region where the Oldest-1 array is deployed. (b) The white serrated line is the axis of the Mariana Trench. The black lines show the Pacific seafloor's age contours (Ma) based on marine magnetic anomaly data (Müller et al., 2008). Orange-shaded area indicates the location of Magellan Seamount Trail (MST). PB, Pigafetta Basin; EMB, East Mariana Basin.

2. Data and Methods

2.1. Data Acquisition and Pre-Processing

As part of the Oldest-1 experiment, we deployed 12 BBOBSs and seven OBEMs by free fall on the seafloor at depths of 5,600–6,100 m in the oldest Pacific Plate (160–180 Ma) (Figure 1, Table S1 in Supporting Information S1) from the Korean RV *Isabu*. The deployment of the instruments was carried out from October to November 2018. Two stations (OL01 and OL02) were deployed in the EMB located southwest of the instrument array site, whereas five stations (OL06, OL07, OL08, OL09, and OL10) were positioned in the PB located to the northeast of the array site. Three stations (OL03, OL04, and OL05) were deployed near the MST, traversing the two basins in our study region. Then, all the instruments were successfully recovered via self-pop-up after a continuous 1-year observation using the Korean RV *Onnuri* from October to November 2019. The BBOBSs used in this experiment were designed by the Earthquake Research Institute (ERI) of the University of Tokyo. The BBOBSs are equipped with CMG-3T broadband seismometers (Güralp Systems Ltd.) and differential pressure gauges (DPG) that have sampling rates of 100 samples/s (Shiobara et al., 2021). During the deployment period, 11 of the 12 BBOBSs provided continuous three-component seismograms and DPG records, while one BBOBS (OL12) recorded DPG data only.

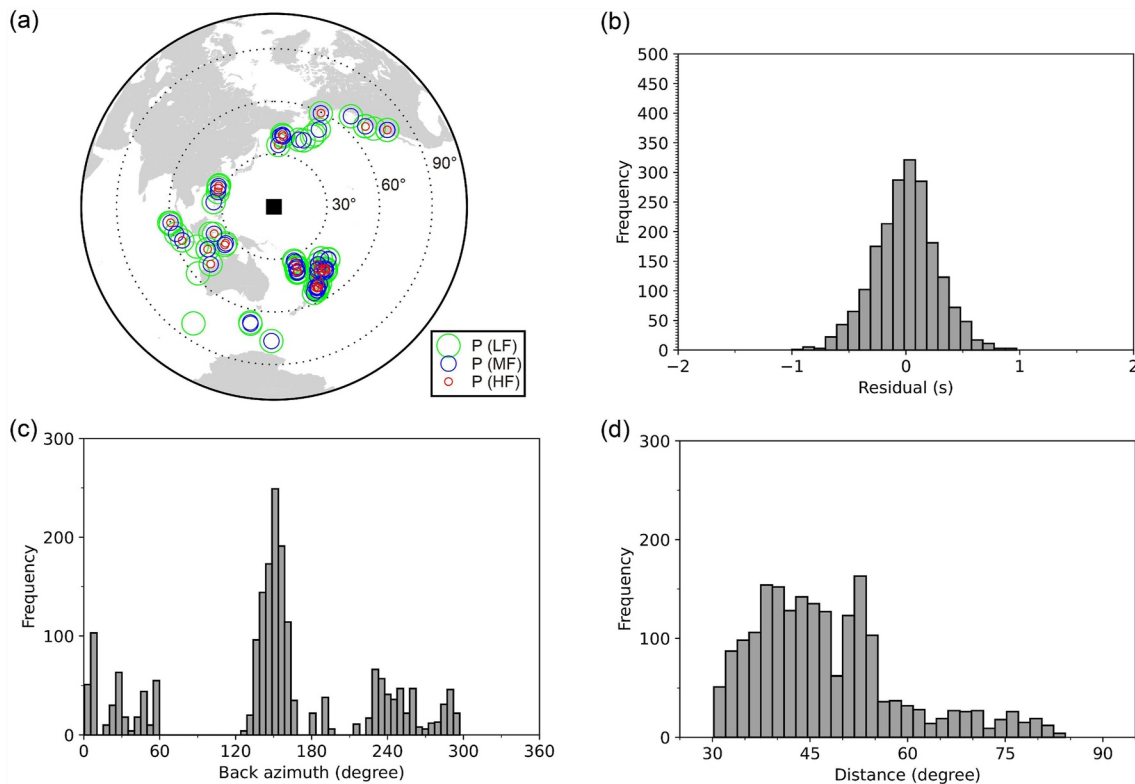


Figure 2. Maps showing the distributions of earthquake and travel time data. (a) The epicenters of the 80 teleseismic events. This study used the 80 teleseismic events for three frequency bands (HF, high frequency; MF, mid-frequency; LF, low frequency). The selected earthquakes for the *P*-wave have magnitudes greater than 5.5 and epicentral distances between 30° and 90°. Each dotted circle indicates a distance interval of 30°. Figure S2 in Supporting Information S1 shows record sections of the filtered teleseismic *P* waveforms of the earthquake occurred on 20 December 2018. (b) The distributions of relative travel time residuals. (c) The distributions of back azimuth. (d) The distributions of distance.

For data pre-processing, time corrections were applied to the data to account for the time difference between the recorder's clock and the GPS clock. Tilt noise was removed from the vertical component seismograms of the 11 BBOBSs by applying a transfer function between the vertical and horizontal components (Kawano, Isse, Kawakatsu, et al., 2023). Following tilt-noise correction, the noise levels of the vertical seismograms were reduced at low frequencies (<0.04 Hz) (Figure S1 in Supporting Information S1). Compliance noise is dominant at frequencies between 0.002 and 0.02 Hz. At frequencies of 0.02–0.1 Hz, the background noise levels of the tilt-noise corrected vertical channels (HHZ) became close to the terrestrial New Low Noise Model (NLNM) of Peterson (1993). More detailed information on the characteristics of background noise in the Oldest-1 array was described by T.-S. Kim et al. (2023).

2.2. Teleseismic Data Sets

Teleseismic *P*-waveforms were collected from the vertical component data of the 11 BBOBSs within an epicentral distance of 30°–90° and earthquake magnitudes greater than 5.5 (Figure 2). The waveforms were band-pass filtered in three frequency bands: (a) 0.0625–0.125 Hz (8–16 s), (b) 0.03125–0.0625 Hz (16–32 s), and (c) 0.02–0.04 Hz (25–50 s) using a second-order Butterworth filter. These frequency ranges are selected to avoid noise peaks at 0.2 Hz (secondary microseism) and 0.002–0.02 Hz (compliance noise) and to take full advantage of the broadband seismic signals (Hung et al., 2000). For quality control, events were selected with an average signal-to-noise ratio (defined as the ratio between the standard deviation of the signal and that of noise in decibels; $20 \times \log_{10}(A_{\text{signal}}/A_{\text{noise}})$, where $A_{\text{signal}} = \sigma(\text{signal})$ and $A_{\text{noise}} = \sigma(\text{noise})$) greater than eight and recorded at three or more stations.

The relative arrival times of *P*-waves were measured by applying the multichannel cross-correlation (MCCC) method to the filtered waveforms (VanDecar & Crosson, 1990). Before the measurement, we calculated the

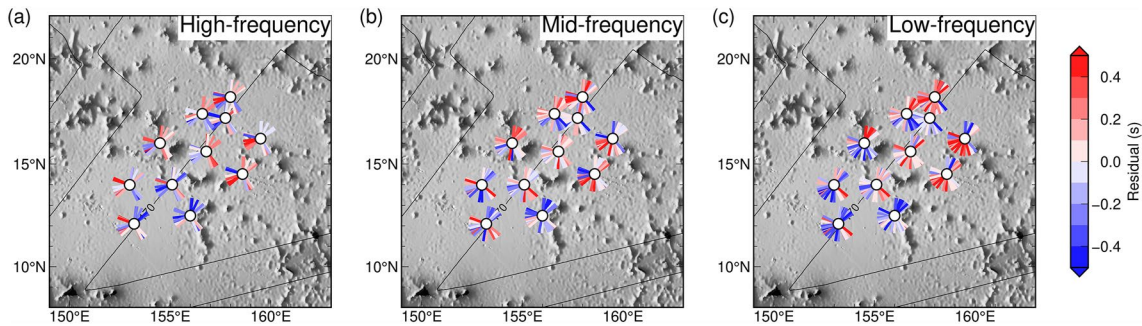


Figure 3. *P*-wave travel time residuals measured at (a) high-frequency (0.0625–0.125 Hz), (b) mid-frequency (0.03125–0.0625 Hz), and (c) low-frequency (0.02–0.04 Hz) bands.

theoretical *P*-wave travel times for the 1-D Preliminary reference Earth model (PREM; Dziewonski & Anderson, 1981) and subtracted them from the corresponding observed seismic traces at the stations. All relative arrival times between any station pair were preliminarily determined as the time delays that led to the maximum cross-correlation coefficients. The optimal relative time delays at individual stations are obtained through a linear inversion with a zero-mean constraint that minimizes the sum of the squared residuals between the differences of the inverted relative time delays for any given station pair and their corresponding cross-correlation measured delays. The associated error (uncertainty) at station *i* is estimated from the residual standard error, namely,

$$\sqrt{\sum_{j=1, j \neq i}^n \text{res}_{ij}^2 / (n - 2)}, \text{ where } \text{res}_{ij} \text{ represents the residual for } i \text{ and } j \text{ pair of } n \text{ stations (Allen et al., 2002). The}$$

measured travel times were relative to the mean travel time for each event, thus minimizing the uncertainties related to the source location and origin time (VanDecar & Crosson, 1990). This process removes information regarding the absolute velocity of the model and results in relative velocity perturbations to an unknown regional average velocity. The travel time residuals were obtained after correcting the relative time delays for demeaned variations in regional bathymetry at the stations. Bathymetric corrections were within ± 0.03 s.

Crustal corrections were applied to account for station-specific delays due to lateral variations in the shallow velocity structure. Because detailed information on the shallow structure is unavailable, the CRUST1.0 model (Laske et al., 2013) is used, including the near-surface structure of the oldest Pacific region constrained by several reflection/refraction profiles (Houtz & Ludwig, 1979). A ray-theoretical crustal correction was applied to the data, which is frequency-independent, given the same raypath. Rays were traced through the CRUST1.0 model (Laske et al., 2013), excluding the sea layer, under the assumption of a fixed geometrical path predicted by PREM (Dziewonski & Anderson, 1981). The crustal travel time difference between the modified CRUST1.0 model and PREM was used as the crustal correction term (Tian et al., 2007). The estimated crustal corrections ranged from ± 0.08 s (Figure S3 in Supporting Information S1). In addition, a frequency-dependent crustal correction was conducted using the cross-correlation of the synthetic waveforms. The synthetics were calculated using the method of H. Kim et al. (2021), assuming a 1-D velocity model for each station from the CRUST1.0 model. The waveforms were filtered using the same band-pass filter applied to the data. The frequency-dependent crustal corrections were within ± 0.2 s for all three frequency ranges (Figure S4 in Supporting Information S1).

The final *P*-wave data set consists of 80 events (1980 travel time residuals) in three frequency bands (high-, mid-, and low-frequency bands). The data set comprises 38 events (417 travel time residuals) in the high-frequency band (8–16 s), 65 events (712 travel time residuals) in the mid-frequency range (16–32 s), and 78 events (851 travel time residuals) in the low-frequency band (25–50 s) (Figure 2a). The travel time residuals showed a Gaussian distribution within ± 1 s (standard deviation of 0.3 s) for *P*-waves across the array (Figure 2b and Figure S5 in Supporting Information S1). The travel time residuals show variations by back azimuths, implying the existence of a complicated Earth structure beneath the array site (Figure 3 and Figure S5 in Supporting Information S1).

2.3. Tomographic Inversion

Relative travel time residual measurements with bathymetric and crustal corrections were used in the tomographic inversion of the upper mantle velocity structure. The observations were weighted by the uncertainty in relative arrival times associated with each trace determined in the application of MCCC method as described

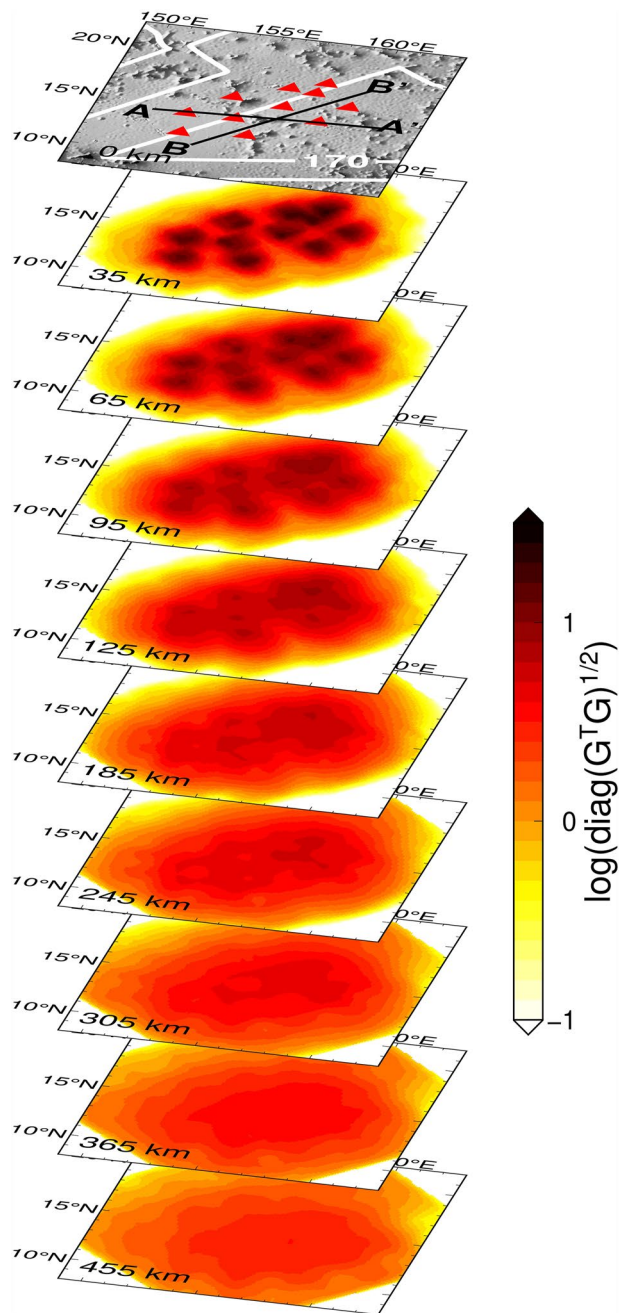


Figure 4. The square root of the diagonal elements of the matrix $\mathbf{G}^T \mathbf{G}$ for P -wave tomographic inversion. It represents the overall sensitivity of finite-frequency travel time data to the slowness variation at each grid node. The values are plotted in a logarithmic scale on nine selected horizontal slices at 35–455 km depth. The top panel shows the locations of the two profiles, AA' and BB'. Map view slices of this figure are presented in Figure S7 of Supporting Information S1.

in Section 2.2. We employed the finite-frequency method for the inversion. We considered the Fréchet derivative of a travel time delay measured from finite-frequency seismic waves concerning 3-D small volumetric perturbations in slowness (reciprocal of the wave speed) throughout the mantle (Hung et al., 2000). The so-called finite-frequency or sensitivity kernel is constructed using the 1-D PREM model (Dziewonski & Anderson, 1981). This was based on the single-scattering (Born) approximation in combination with body-wave propagation and paraxial ray approximation (Hung et al., 2000). The formulation of the kernel adequately describes the wave-front healing and diffraction effects on finite-frequency seismic wave propagation and the resulting 3-D frequency-dependent sensitivity off the raypath. The ray-bending effects are neglected in the kernel calculation based on the PREM. Such effects are expected to be minimal because cross-correlation travel time measurements are mainly unaffected by the ray-bending effects for relatively small velocity perturbations, which are typically obtained from teleseismic body-wave travel time tomography (root mean square of velocity perturbations <6%) (Yang & Hung, 2005).

A multiscale parameterization method was adopted in this study to recover the model. Instead of directly solving the model parameters specified at discretized nodes, the model vector \mathbf{m} and associated data kernel \mathbf{G} were transformed in wavelet expansions using the 3-D primary (\mathbf{W}) and dual wavelet bases, respectively (Hung et al., 2011). Similarly, the model (\mathbf{Wm}), which is decomposed and expressed as a series of wavelet coefficients at various scales, can be achieved by a damped least squares solution of the same inverse problem $\mathbf{GW}^{-1}\mathbf{Wm} = \mathbf{d}$, where \mathbf{W}^{-1} is the inverse primary wavelet transform, \mathbf{GW}^{-1} is the transformed data kernel, and \mathbf{d} is the data vector. The final model vector was constructed by applying the inverse primary wavelet transform to \mathbf{Wm} , which synthesizes the resulting wavelet coefficients from the coarsest to finest scales to maintain an inherently nonstationary, data-adaptive resolution of the model at different scales (Hung et al., 2011). Hung et al. (2011) provide more details on multiscale parameterization.

The study region was parameterized into a grid within an area of $15^\circ \times 15^\circ$, extending 5–485 km in depth (Figure S6 in Supporting Information S1). We assigned 33 nodes along each horizontal direction (NE–SW) and 17 nodes along the vertical direction, which gave rise to grid sizes of 50 km, 50 km, and 30 km in three dimensions, respectively. The model parameterization was selected after considering the overall sensitivities of the data (P -wave travel time) contributing to the grid nodes. The spatial distribution of the diagonal values of the matrix $\mathbf{G}^T \mathbf{G}$, where \mathbf{G}^T is the transpose of \mathbf{G} , can be used as a proxy to visualize the overall sensitivity of the kernel contributing to a grid node. The uppermost ~400 km of the mantle was sampled evenly by the kernels (Figures 4 and 5). A damping parameter is determined by considering the trade-off between variance reduction and the model norm (Figure S8 in Supporting Information S1). A slightly higher damping value (1,000) for the final model was chosen compared to that at the turning point to reduce the model norm and suppress unrealistically large amplitude ranges of the velocity perturbation. We note that our final P -wave velocity model presents relative velocity perturbations at each depth to an unknown regional average P -wave velocity, resulting from the demeaning process in the measurement of relative travel time residuals.

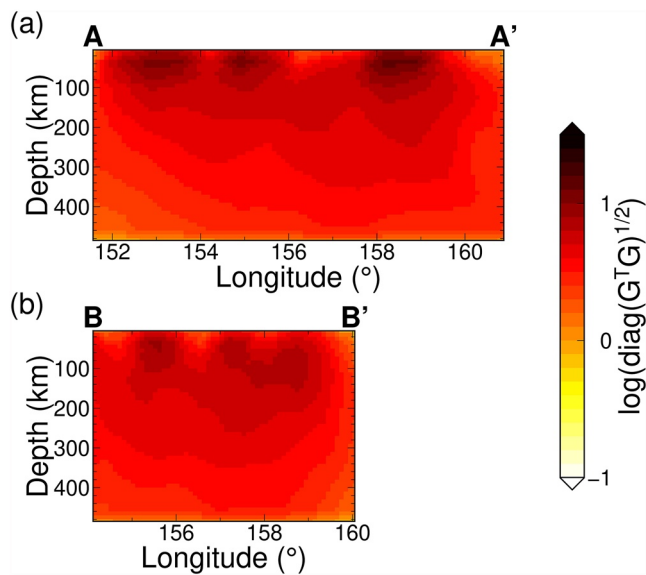


Figure 5. Cross-sections of the square root of the diagonal elements of the matrix $G^T G$ along (a) profile AA' and (b) profile BB'. The top panel of Figure 4 shows the locations of the two profiles AA' and BB'.

3. Results

3.1. Resolution Test

A series of checkerboard tests were performed to evaluate the spatial resolution of the V_p model. Input models were constructed using alternating velocity perturbations with amplitudes of $\pm 3\%$ for the V_p model. Synthetic relative travel time residuals were then calculated by multiplying the hypothetical models with the G matrix constructed from the actual data with 3-D finite-frequency kernels. The synthetic data used the same source-receiver configuration as the actual data. Gaussian random noise comparable to the average uncertainty of the travel time measurement (0.08 s) was added to the synthetic data. The inversion was then performed by adopting the same inversion process as in the case of actual data.

The checkerboard test for the V_p model showed that velocity anomalies with lateral and vertical dimensions of ~ 250 and ~ 210 km, respectively, could be resolved well down to a depth of ~ 400 km (Figure S9 in Supporting Information S1). Checkerboard anomalies generally recovered well in regions where $\text{diag}(G^T G)^{1/2}$ values were more significant than 0.13% of the overall maximum. The amplitude recovery in input and output checkerboard models was 50% on average. The pattern correlation between input and output was 0.71 on average for the six depth ranges within 95–335 km, as shown in Figure S9 of Supporting Information S1. Comparing the checkerboard test results with

resolution matrix proxy $G^T G$ (Figure 4), we displayed the V_p model only at nodes where $\text{diag}(G^T G)^{1/2}$ values exceeded 0.13% of the overall maximum at all nodes.

3.2. Tomographic Model

The V_p model with a ray-theoretical crustal correction was used for presentation and interpretation. The model's main characteristics in terms of the location and geometry of velocity anomalies did not vary significantly for depths greater than 95 km, regardless of the choice of ray-theoretical or frequency-dependent crustal correction schemes (Figures 6 and 7; Figure S10 in Supporting Information S1). A comparison between the two models only shows minor changes in the amplitude of the V_p anomalies. This is because shallow structures depend more on crustal corrections and the choice of near-surface velocity models than deep structures. Furthermore, near- and middle-field influences on the travel time sensitivity kernel can contribute down to a depth of one wavelength and can be significant within a depth of $0.5 \times$ wavelengths near the source or receiver for P -waves (Favier et al., 2004). Some local field influence is expected to be down to a depth of ~ 80 km, considering the dominant wavelength of P -waves used in this study.

The finite-frequency V_p model showed seismic mantle structures across the oldest Pacific region (Figures 6 and 7). At the lithospheric depth range (35–65 km), our model reveals relatively fast- V_p perturbations (3%–4%) beneath station OL05, located in the southern part of the array site. Whereas, other portions of the array site predominantly exhibit relatively slow- V_p perturbations. A more detailed discussion of the lithospheric V_p structure cannot be conducted as the model at such depths may suffer from limited resolution and potential bias by using long-period teleseismic P waves. Nonetheless, the observed complex 3-D V_p structure of the oldest Pacific lithosphere may be attributed to its intricate evolutionary history.

For depth ranges of 95–305 km, the amplitude of velocity anomalies is $\pm 3.6\%$ on 1–99 percentiles or $\pm 3.1\%$ on 2.5–97.5 percentiles over the nodes where $\text{diag}(G^T G)^{1/2}$ is greater than 0.13%. Beneath the PB, fast V_p values (denoted as F1) with a radius of ~ 200 km were observed at depths of 95–185 km. The southwestern part of the array site shows a slow V_p anomaly (S1) at depths of 95–305 km close to the MST. The S1 anomaly is elongated in the southeast-northwest direction along the MST and has a width of ~ 200 km and a length of ~ 500 km. The northwestward extension of S1 was found to be the strongest at depths of 125–245 km, while it was restricted to the southeast at deeper depths. To the east, another slow V_p anomaly (S2) is present 95–305 km beneath the oldest part of the Pacific seafloor (>170 Ma). The amplitude of the S2 anomaly is found to be the strongest (-3

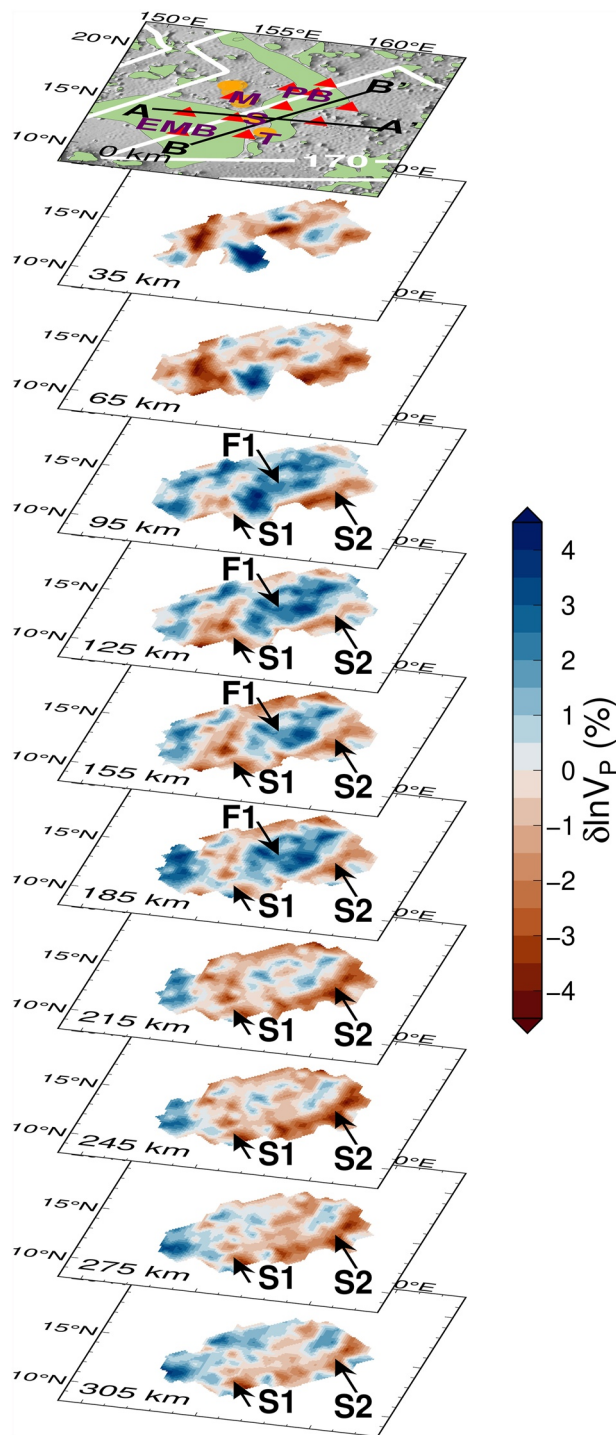


Figure 6. The final model of $\delta \ln V_p (= \delta V_p / V_p)$ for 10 horizontal layers at 35–305 km depths. The model at nodes with a $\text{diag}(\mathbf{G}^T \mathbf{G})^{1/2}$ values exceeding 0.13% of the overall maximum at all nodes is shown. The top panel shows the locations of the two profiles AA' and BB'. The global distribution of large igneous provinces is shown as green-colored areas (Coffin et al., 2006). Map view slices of the final model are presented in Figure S11 of Supporting Information S1. Orange-shaded area indicates the location of Magellan Seamount Trail (MST). PB, Pigafetta Basin; EMB, East Mariana Basin.

to -4%) for depths of 215–275 km and was elongated in shape, trending southwest-northeast, roughly parallel to the western edge of the 170 Ma age contour.

3.3. Synthetic Tests

A series of synthetic tests were performed to ensure that our data could resolve the observed $\delta \ln V_p$ anomalies F1, S1, and S2. In the synthetic tests, $\delta \ln V_p$ perturbations of $+2\%$ for F1 and -2% for S1 and S2 were adopted to represent the average $\delta \ln V_p$ amplitude of the observed anomalies in the final V_p model (Figures 6 and 7). The model includes three velocity anomalies: a cylindrical, fast V_p structure ($\delta \ln V_p = +2\%$) with a radius of 200 km at depths of 90–210 km, and two elongated slow V_p structures ($\delta \ln V_p = -2\%$) at depths of 90–315 km (Figures 8 and 9). The resulting images show that the overall shapes of the anomalies generally recovered well, although they were slightly smeared along the southeast owing to the concentration of events in the southeast.

Further tests were conducted to verify whether velocity artifacts appeared surrounding the input model's strong slow or fast V_p anomalies. First, we examined whether a fast V_p anomaly in the center of the array (F1) could produce slow V_p structures (S1 and S2) surrounding PB (Figure S13 in Supporting Information S1). The recovered synthetic model shows that fast V_p anomaly ($\delta \ln V_p = +2\%$) can generate slow- V_p anomaly in its vicinity as an artifact, but its amplitude is less than 10% of that in the final model. We also considered a case in which slow- V_p anomalies ($\delta \ln V_p = -2\%$) in the eastern and southern parts of the array (S1 and S2) could produce a fast V_p structure in the center of the array (F1) as an artifact (Figure S14 in Supporting Information S1). The synthetic test result shows that the maximum amplitude of the artifact fast- V_p anomaly is less than 10% of the fast velocity anomaly in the final V_p model. This suggests that the observed features were robust.

Finally, additional tests are conducted to verify the vertical extent of the observed slow- V_p anomaly. Two synthetic models were constructed such that the model had fast- V_p ($\delta \ln V_p = +2\%$) at the center of the array for 90–210 km depth in common and slow- V_p ($\delta \ln V_p = -4\%$) around the fast anomaly at different depths (Figure S15 in Supporting Information S1). The first synthetic model had a slow- V_p anomaly for 210–285 km, where the S2 anomaly was found to be the most potent (Figures S15a and S15b in Supporting Information S1). Another model had an elongated slow- V_p anomaly at depths of 90–165 km around the fast anomaly (Figures S15c and S15d in Supporting Information S1). Both recovered synthetic models show inevitable vertical smearing, which requires careful interpretation of the final model. However, the elongated slow- V_p model shown in Figures 8 and 9 provides a better explanation for the observed strong amplitude of slow- V_p at overall depths of ~ 100 –300 km in the final V_p model.

4. Discussion

4.1. Robustness of the V_p Model

The robustness of the final V_p model was assessed by testing for systematic bias in measurements of the relative travel time residual of stations (OL07, OL05, and OL04) located on/near thick sediment and crust (Figures S3a and S3b in Supporting Information S1). Tomographic inversions were performed using only 10 stations, excluding one of the three (Figure S16 in Supporting

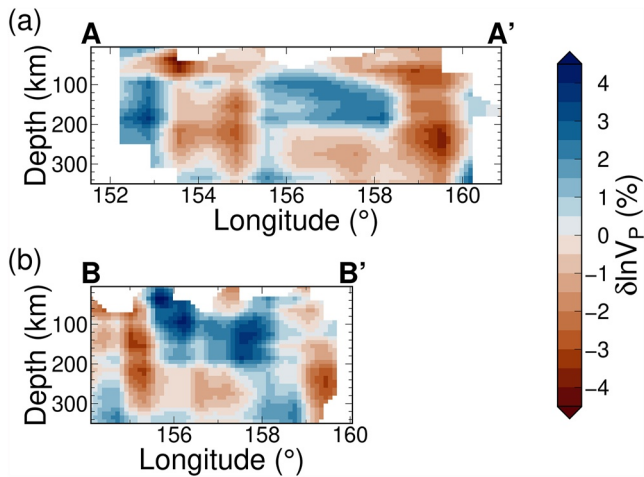


Figure 7. Cross-sections of the final model of $\delta \ln V_p$ along profile AA' (a) and profile BB' (b). The model at nodes with a $\text{diag}(\mathbf{G}^T \mathbf{G})^{1/2}$ values exceeding 0.13% of the overall maximum at all nodes is shown. The top panel of Figure 6 shows the locations of the two profiles AA' and BB'.

Information S1). Relative travel time residuals were measured for the 10 selected stations. Therefore, any potential bias in the measurements associated with each of the three stations was excluded. The 10-station V_p models were displayed only at nodes where $\text{diag}(\mathbf{G}^T \mathbf{G})^{1/2}$ values exceeded 0.13% of the overall maximum at all nodes, as in the 11-station V_p model (Figures 6 and 7).

The 10-station model, excluding station OL07, generally showed features consistent with the 11-station model (Figure S16a in Supporting Information S1). At depths of 215–305 km, a weak slow- V_p anomaly below station OL07 in the 11-station model (Figure 6) disappeared or weakened in the 10-station model. The model resolution decreases beneath station OL07, primarily for depths less than 95 km, which is not our main target in this study.

When the data from station OL05 were removed, only a portion of the array site was resolved, except for locations near station OL05 (Figure S16b in Supporting Information S1). In the 10-station model without station OL05, the amplitude of the S1 anomaly became weaker at depths of 125–155 km. A weak (neutral) V_p anomaly beneath station OL07 for depths of 215–245 km in the 11-station model (Figure 6) changed into a slower V_p anomaly in the 10-station model (Figure S16b in Supporting Information S1). However, the

overall configuration of the significant anomalies (S1, S2, and F1) from the 11-station model is clearly observed in the 10-station model (Figure S16b in Supporting Information S1).

The model without station OL04 showed a reduction in resolution near station OL04 for a shallow depth of fewer than 95 km. The $\mathbf{G}^T \mathbf{G}$ resolution threshold partly masked this area. However, the slow anomaly (S1) persisted at depths of 95–215 km in the 10-station model without OL04. At depths of 275–305 km, the resolution for the southwestern part of the array was reduced by excluding station OL04 (Figure S16c in Supporting Information S1). However, the major anomalies of the tomography models (S1, S2, and F1) from the 11-station model were still clearly observed in the 10-station model (Figure S16c in Supporting Information S1).

The tests mentioned above demonstrate that the major characteristics of the tomography model (S1, S2, and F1) from the 11-station model (Figures 6, 7, and Movie S1) remain mostly unaffected by the exclusion of data from stations on top of the relatively thick sediment and crust layers (Figure S16 in Supporting Information S1). This may indicate that the effect of the shallow structure is insignificant in revealing a mantle structure >95 km in our tomography results.

4.2. Comparison With Global Models

We compared our model with several global models, including PAC-age (Isse et al., 2019), SPiRaL (Simmons et al., 2021a), SPani (Tesoniero et al., 2015a), HMSL (Houser et al., 2008b), and SP12RTS (Koelemeijer et al., 2016a) (Figure 10 and Figure S17 in Supporting Information S1). Note that these models are constrained incorporating surface wave data, thus providing better vertical resolution down to the lithosphere-asthenosphere depth range compared to global models that rely solely on teleseismic body waves.

The PAC-age model (Isse et al., 2019) presents a radially anisotropic S -wave model of the upper mantle beneath the Pacific Ocean. In our study area, this model mostly reveals a fast S -wave velocity anomaly at depths ranging from 50 to 200 km, except the region south of our array site (Figure 10b and Figure S17a in Supporting Information S1). Notably, our observation of the fast- V_p anomaly (F1) at depths of 95–185 km falls within the depth range of the fast- V_s anomaly in the PAC-age model. While the localized slow-velocity anomalies (S1 and S2) in our model are not clearly visible in the PAC-age model, the slow- V_s anomaly observed south of the array site in the PAC-age model suggests a potential association with the slow-velocity anomalies in our model.

Other global models such as SPiRaL (Simmons et al., 2021a), SPani (Tesoniero et al., 2015a), and SP12RTS (Koelemeijer et al., 2016a) predominantly exhibit fast- V_s and fast- V_p anomalies at depths shallower than ~150 km in our study area (Figures S17b–S17d in Supporting Information S1). The HMSL model (Houser et al., 2008b)

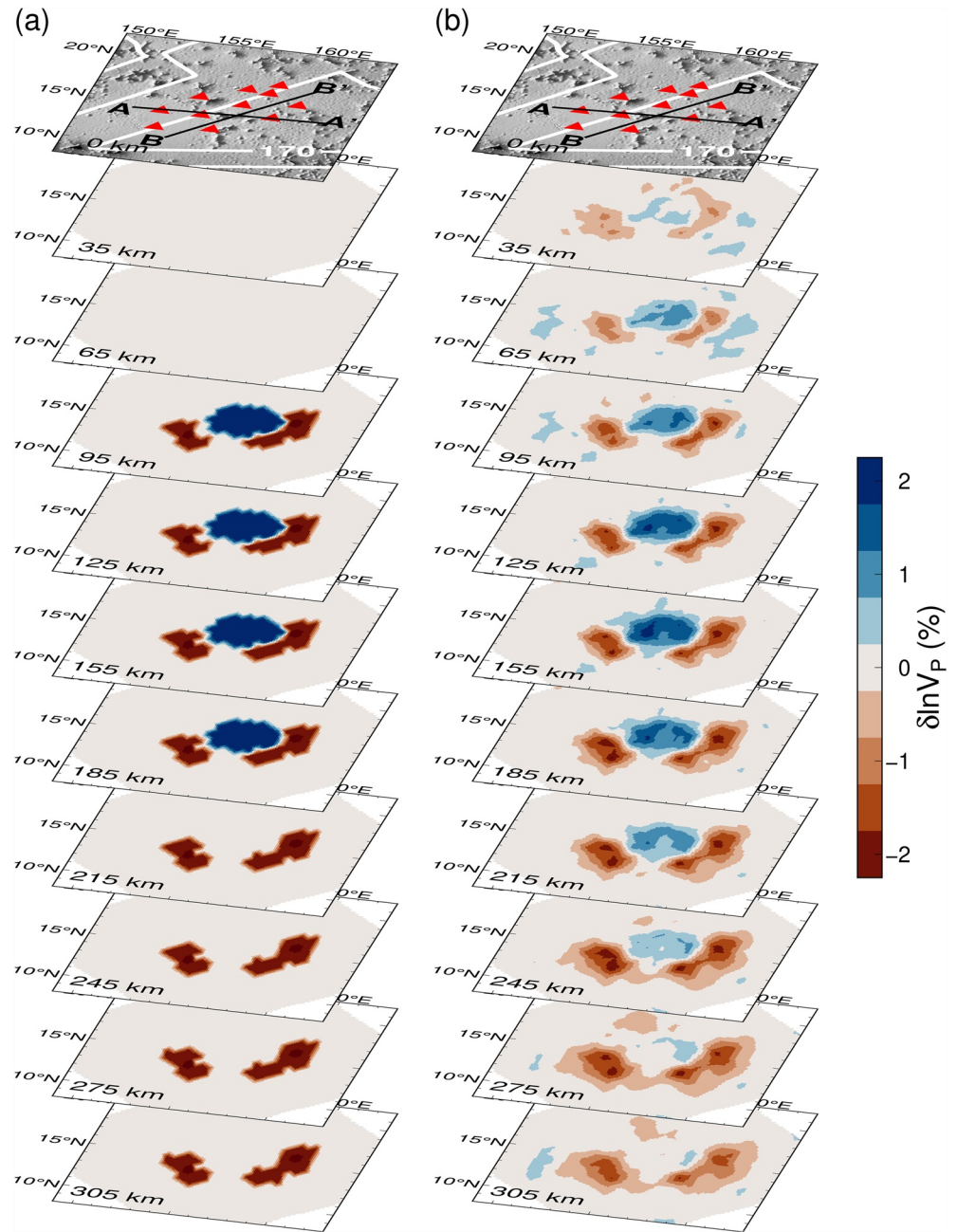


Figure 8. Synthetic test results for the observed V_p anomalies ($\delta \ln V_p = \pm 2\%$) such as F1, S1, and S2. Horizontal slices of the input model (a) and the output model (b) are shown. Map view slices of (a) and (b) are presented in Figure S12 of Supporting Information S1.

in particular displays fast- V_s and fast- V_p anomalies at a depth of 155 km, while also featuring slow- V_s and slow- V_p anomalies at the southeastern part of the array site, at a depth of 66 km (Figure S17e in Supporting Information S1).

For depths deeper than ~ 150 km, the global models exhibit distributions of slow- V_s and slow- V_p anomalies that are mainly centered on the southeastern parts of our study area, although their depth ranges vary among models. The SPiRaL model presents pronounced slow- V_p and slow- V_s anomalies at the southeastern parts of the array site, ranging from depths of 185–355 km (Figure 10c and Figure S17b in Supporting Information S1). Similarly, the SPani model shows slow- V_s and slow- V_p anomalies centered on the southeastern part of the array site from depths of 175–300 km (Figure S17c in Supporting Information S1). The SP12RTS model exhibits

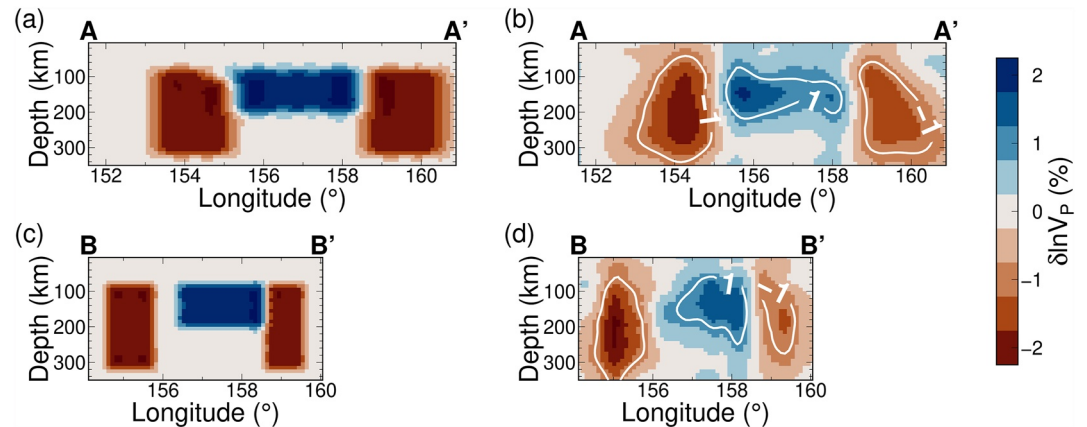


Figure 9. Cross sections of the synthetic test results along profile AA' and profile BB'. The top panels of Figure 8 show the locations of the two profiles AA' and BB'. Vertical slices of the input model (a) and output model (b) along profile AA' are shown. Vertical slices of the input model (c) and output model (d) along profile BB' are shown. White lines in figures (b) and (d) indicate $\pm 1\%$ contours of the recovered (output) P -wave model.

slow- V_s and slow- V_p anomalies within the southeastern part of the array site at depths between 170 and 300 km (Figure 10d and Figure S17d in Supporting Information S1). The HMSL model reveals slow- V_s and slow- V_p anomalies at the southern part of the array site, ranging from depths of 250 and 350 km (Figure S17e in Supporting Information S1).

Overall, the depth range of fast velocity anomalies in the global models (Figure S17 in Supporting Information S1) is generally comparable with our observation of the fast- V_p anomaly (F1) extending from 95 to 185 km in our model. Furthermore, our observation of slow- V_p anomalies (S1 and S2) at the southern and eastern parts of the array site is consistent with the distribution of slow-velocity anomalies in the global models. However, the S1 and S2 extend over a broader vertical range, spanning from 95 to 305 km, compared to the slow-velocity anomalies in the global models. The observed differences should arise from the lack of in situ OBS observation at our study region in the global models. In addition, different datasets and parameterization schemes, and discrepancies in modeling assumptions and choices can contribute to the differences.

We further checked several global lithospheric thickness models, and those models show somewhat large variation in the estimates of the lithospheric thickness over the oldest Pacific region (Figure S18 in Supporting Information S1). For example, the model WINTERC-G (Fullea et al., 2021) shows lithospheric thickness of 70–160 km over our study region, and a thick lithosphere (110–160 km) is present at the northwestern and south-eastern edges of the array site (Figure S18a in Supporting Information S1). Another model derived from upper mantle V_{SV} model, which is CAM2016 V_{SV} (Priestley et al., 2018), provides lithospheric thickness of 100–130 km at the central part of the array site (Figure S18b in Supporting Information S1). The LITHO1.0 model (Pasyanos et al., 2014) exhibits thicker lithosphere estimates for the oldest Pacific region, up to 210–240 km in the south-eastern part of the array site (Figure S18c in Supporting Information S1). Additionally, the model of Conrad and Lithgow-Bertelloni (2006) shows lithospheric thickness of approximately 100 km for our study region (Figure S18d in Supporting Information S1). The discrepancy in thickness estimates among the global models may stem from different data sources such as seismic tomography, gravity anomalies, and heat flow measurements, as well as different methodologies, modeling techniques, and assumptions.

The observed fast V_p anomaly (F1) centered beneath the PB at depths of 95–185 km may indicate the presence of localized thick lithosphere beneath the region. However, due to the relative nature of our model and the lack of information regarding the regional average P -wave velocity, accurately determining the 3-D lithospheric thickness remains challenging. Recent studies (Kawano, Isse, Takeo, et al., 2023; H. Kim et al., 2020) have provided useful constraints on the complex lithospheric structure of the oldest Pacific Plate. Using the same array data, broadband Rayleigh-wave dispersion analysis provides an array-averaged 1-D V_s profile, showing a lithospheric thickness of approximately 80–100 km in the oldest Pacific region (Kawano, Isse, Takeo, et al., 2023). An analysis of the Oldest-1 OBEM data provides a 1-D conductivity profile over the region, indicating a thicker resistive lithospheric structure (H. Kim et al., 2020). The 3-D variation of lithospheric

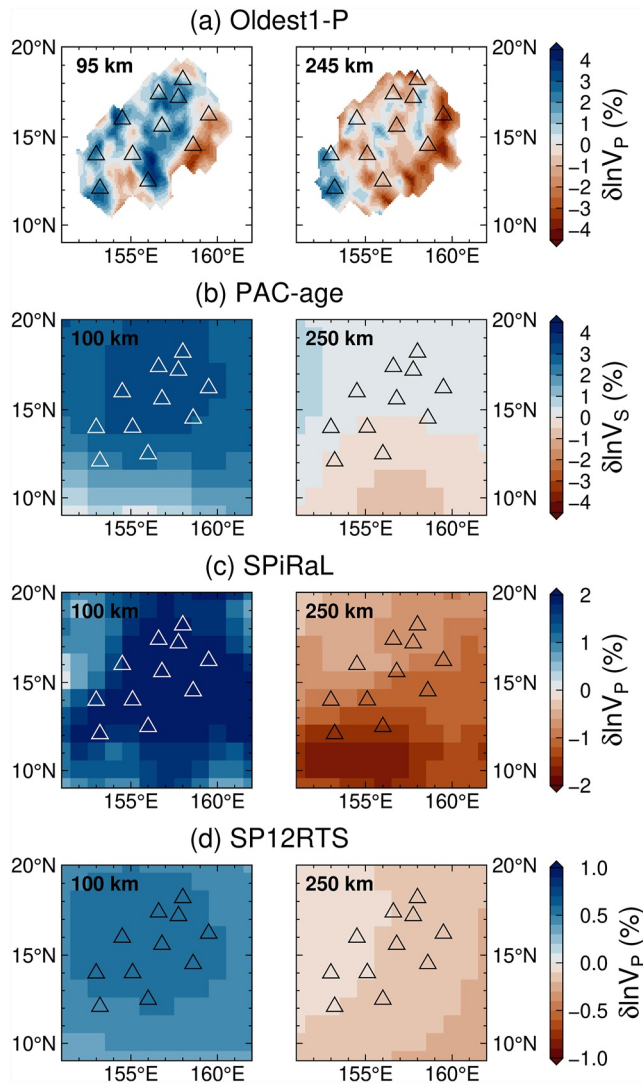


Figure 10. Comparison of the global tomographic models such as PAC-age (Isse et al., 2019), SPiRaL (Simmons et al., 2021a), and SP12RTS (Koelemeijer et al., 2016a) with the V_p model obtained from this study (Oldest1-P) at two depths, approximately 100 and 250 km. (a) V_p model derived from this study (Oldest1-P), (b) PAC-age model (Isse et al., 2019), (c) SPiRaL (Simmons et al., 2021a), and (d) SP12RTS (Koelemeijer et al., 2016a).

thickness of the oldest Pacific can be intricate, and future joint analysis involving surface waves and EM data may offer further insights into this variation.

4.3. Thermochemical Properties of the Model

Various factors affect the seismic velocity of the upper mantle. Among these factors, the dependence of seismic velocities on temperature (Cammarano et al., 2003) has typically been employed to infer the results of tomography models (e.g., Hung et al., 2004; Isse et al., 2019; Schlömer et al., 2017). Other mechanisms, such as the presence of partial melt (Hammond & Humphreys, 2000), water (Karato & Jung, 1998), heterogeneity in composition (e.g., an abundance of olivine; C.-T. A. Lee, 2003), and grain size (Faul & Jackson, 2005) are also known to cause seismic velocity perturbations.

In this study, we first considered the effects of temperature and partial melting on the observed slow- V_p anomalies (S1 and S2). Assuming that elevated temperature alone is the cause, the $\sim 7\%$ peak-to-peak amplitude of the observed velocity anomalies corresponds to a lateral temperature variation of up to 520–1120°C (99 percentile for each depth slice) as a function of depths, for a typical 1300°C mantle adiabat (Cammarano et al., 2003). The depth dependency of the temperature anomaly arises due to the decrease in temperature sensitivity of V_p with increasing depths (Cammarano et al., 2003). To estimate the absolute mantle temperature of the velocity anomalies, we assumed that the 1-D reference absolute temperature for our model corresponds to a typical mantle adiabat with a potential temperature of 1300°C (Cammarano et al., 2003). Under these assumptions, we attribute the lowest velocities to the presence of extra hot material with a temperature increase of 260–560°C depending on the depth, relative to the reference absolute mantle temperature. Similarly, the highest velocities are likely caused by the presence of cold material with a temperature decrease of 260–560°C depending on the depth, relative to the reference absolute mantle temperature.

We found that the elevated absolute mantle temperature for slow- V_p anomalies partly exceeds the mantle dry solidus (Hirschmann, 2000) at depths of 95–305 km. This suggests the presence of melt in the upper mantle below the oldest Pacific. The presence of melt for the slow- V_p anomalies becomes even more likely if we consider mantle adiabat with a higher mantle potential temperature of 1600°C, with an estimated temperature increase of up to 200–360°C for the 1600°C mantle adiabat (Cammarano et al., 2003). However, the lack of information on the reference absolute velocity of the model may lead to uncertainty in the estimation of the absolute temperature and melt in this study. It is important to note that differential travel-time

tomography constrains lateral velocity gradients, which are then used to estimate temperature gradients, rather than absolute velocities. In extreme case, fast-velocity anomalies could be considered as a normal mantle and slow-velocity anomalies could be twice as large and vice versa.

It has been suggested that the amount of melt present during mantle melting is approximately 0.1% (McKenzie, 1985). A melt fraction of 0.1% may account for about 0.36% P -wave velocity reduction (Hammond & Humphreys, 2000). Then, considering the V_p reduction due to melting content and temperature together, temperature increases of 230–500°C may explain the slow- V_p anomaly in the final model for the 1300°C mantle adiabat (180–330°C for 1600°C mantle adiabat). If the melt fraction in the asthenosphere exceeds McKenzie's (1985) estimate, the upper limit of melt required to explain the negative velocity anomalies observed in our study (up to 3.6%) would be higher. Assuming a linear relationship between melt fraction and velocity reduction, a melt fraction of approximately 1% could be present in the asthenosphere to account for the observed velocity anomalies from melt alone. However, a strong dependency of seismic velocities on melt geometry may contribute to a

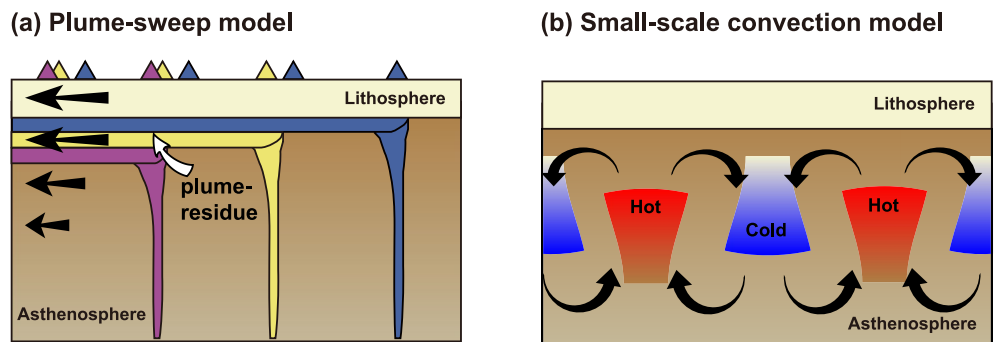


Figure 11. Schematic figures for possible scenarios. (a) The schematic figure for the “plume-sweep” model was modified after Jackson et al. (2010). This model implies that multiple plume activities during the Pacific Plate’s evolution left behind a dry, viscous, and rigid melt residue at the base of the lithosphere of the oldest Pacific. Colored triangles show volcanic islands produced from plumes of the same color due to plate motion. (b) Schematic figure for the “small-scale convection” model, modified after Eilon, Zhang, et al. (2022).

source of error in these estimates. Furthermore, the presence of melt, including pre-melting, can cause physical dispersion through seismic attenuation and may result in considerable heterogeneity in the observed seismic velocity.

There can also be unaccounted seismic anisotropy that may have contributed to the observed back-azimuthal variation of P -wave traveltimes residuals and amplitude of anomalies in the tomography models (Babuška et al., 1984; Babuška & Plomerová, 2006; Eberhart-Phillips & Mark Henderson, 2004; Eken et al., 2012). A recent study has revealed a moderate azimuthal seismic anisotropy (1.6%–2.8%) at depths shallower than 50 km in the oldest Pacific region, as determined by a Rayleigh-wave dispersion analysis from the Oldest-1 experiment (Kawano, Isse, Takeo, et al., 2023). Additionally, recent work by H. Lee et al. (2021) showed that the low-velocity anomaly behind the Alboran slab could be partially (by ~ 1 –2% dV_p/V_p) explained by seismic anisotropy.

In addition, it is likely that water infiltration through the fracture zones of the old Pacific Plate resulted in localized enhancement of hydration of the upper mantle and contributed to the slow- V_p anomalies observed. Local hydration of the middle to deep parts of the oceanic lithosphere may occur as the plate passes over plumes, as upwelling and solidifying magmas release water that hydrates the surrounding mantle (Seno & Yamanaka, 1996). Increase of water content in the upper mantle reduces seismic velocities through anelastic relaxation by several percent (Karato, 1995; Karato & Jung, 1998). In addition, increased water content lowers the melting temperature of mantle rocks and increases the degree of mantle melting, thereby producing slow- V_p anomalies (Asimov & Langmuir, 2003).

On the other hand, our model shows a structure of relatively higher seismic velocities (2%–4%) beneath the PB (F1) at depths of 95–185 km. Many tomography studies commonly interpret seismically fast features at such depth ranges as cold and rigid lithosphere (e.g., Hung et al., 2011). However, the vertical extent of the F1 anomaly (185 km) was more profound than that estimated for the old oceanic lithosphere of 160–180 Myr. According to the half-space cooling model, assuming a basal isotherm of 1100°C, the lithospheric thickness was estimated to be ~ 145 km (Fowler, 2004). In this case, the vertical extent of the F1 anomaly is approximately 40 km deeper than the estimated lithospheric thickness. In addition, the vertical extent of the F1 anomaly was found to be much deeper than the lithospheric thickness (~ 90 km) estimated for the oceanic lithosphere of 160–180 Myr in the plate model (McKenzie et al., 2005).

4.4. Plume-Sweep Model

The “plume-sweep” model can describe the first possible scenario in the oldest Pacific. During the evolution of the Pacific Plate, several plume-activities have modified the upper mantle of the oldest Pacific (Figure 11a). As the oldest Pacific Plate traversed several hotspots in the South Pacific (e.g., Samoa, Rarotonga, Arago, and Macdonald) (Wessel & Kroenke, 2008), the fast- V_p anomaly (F1) in our final velocity model may represent highly viscous and rigid melt residues accreted beneath the lithosphere. Our tomography model is consistent with the results of the electromagnetic study on the oldest Pacific seafloor using seven OBEMs collocated with

our BBOBS locations of the Oldest-1 array. Analysis of the OBEM data provided a 1-D conductivity profile, suggesting a thick resistive lithospheric structure (H. Kim et al., 2020).

The heterogeneous geochemical composition of the MST lavas indicates that they were formed either by the Rarotonga plume activity on the Pacific lithosphere that had previously been metasomatized by the earlier Arago plume material or by partial melting of a single heterogeneous plume (Wei et al., 2022). When an oceanic plate passes over a series of hotspot regions for several tens of millions of years, a thick, highly viscous, and seismically fast structure can be produced at the base of the lithosphere because of the melt depletion and dehydration of plume-related residual materials (Phipps Morgan, Morgan, & Price, 1995). The geochemical affinities of the Samoan volcanoes with the three hot spots in the South Pacific (Rarotonga, Arago, and Macdonald) support the presence of depleted viscous plume residues beneath the Pacific lithosphere (Jackson et al., 2010).

The depleted restite root has been suggested by Yamamoto and Phipps Morgan (2009) for the sublithospheric structure of Hawaii. In addition, there are several other places on Earth where the presence of a thick dehydrated plume residue at the base of the lithosphere has been suggested, including Hawaii (Le et al., 2022), OJP (Isse et al., 2021; Tharimena et al., 2016), Réunion and Mauritius (Hable et al., 2019), and the Tristan da Cunha archipelago (Schlömer et al., 2017). In particular, previous geochemical analysis results have provided evidence that the flood basalts in our study region were genetically linked to the OJP (e.g., Castillo et al., 1994; Mahoney, 1987), which suggests that they might have been fed by lateral lava flow from the mantle plume that generated the OJP by a magma plumbing system or sublithospheric channeling (Ernst, 2014). This process may have provided an additional source of residual plume material that underplated the oldest Pacific lithosphere.

In this scenario, the observed slow- V_p anomalies (S1 and S2) correspond to the asthenosphere, with a relatively slower V_p than the seismically fast plume residue. Possibly, but not necessarily, the slow- V_p structures (Figures 6, 7, and Movie S1) may represent the elevated temperature, melt, and volatile content of the Jurassic fossil plume, which has been suggested for the birth of the Pacific Plate (Pavoni, 2003). Strong coupling between the asthenosphere and lithosphere beneath the oldest Pacific seafloor is required to entrain the Jurassic plume to its current location in the western Pacific for a long time (~ 180 Myr). However, it can be challenging to maintain a high degree of coupling between the lithosphere and asthenosphere in an oceanic environment owing to the thin lithospheric thickness ($< \sim 145$ km), the low viscosity of the asthenosphere (Ricard et al., 1991), and low viscosity of the mantle plume. On the other hand, the presence of a Jurassic plume below the oldest Pacific may support a plume-fed asthenosphere in which asthenospheric flow derives plate motion (Phipps Morgan, Morgan, Zhang, & Smith, 1995).

If the slow anomaly is a normal asthenosphere, the observed lateral velocity contrast of $\sim 7\%$ is significant and difficult to be solely explained by a compositional variation for the depleted melt residue. Jordan (1979) estimated that the removal of 10% basaltic melt from peridotite would cause a 1% increase in V_p , suggesting that an extreme degree of melt extraction ($\sim 70\%$) would be needed to generate the thick residue beneath the oldest Pacific. Other studies have proposed compositional explanations for velocity anomalies in different regions. For example, Rost and Williams (2003) attributed a $\sim 10\%$ elevation in V_p to a plume residue of extensive garnet enrichment by mineralogic modeling. Isse et al. (2021) proposed that 1%–2% higher S -wave velocities beneath OJP lithosphere could have a compositional cause, interpreted as melt residues from a mixed peridotite-pyroxenite source in a thermochemical plume. Allen et al. (2002) interpreted high V_p anomalies of 2% as the result of the extreme degree of melt extraction necessary to generate the thick (46 km) crust in central Iceland. Further investigation of physical properties, such as V_s and V_p/V_s ratios of the study region, may provide additional constraints in understanding the origin of our observed V_p structure.

4.5. Small-Scale Convection Model

Taking the observed slow and fast V_p anomalies together, the possibility of small-scale convection (SSC) cannot be excluded (Movie S1 and Figure 11b). It has been suggested that SSC arises from instability at the bottom of the mature oceanic lithosphere when its thickness exceeds a critical value (Ballmer et al., 2007). It has the form of convective rolls aligned parallel to plate motion and removes the bottom of the depleted harzburgite layer by replacing it with underlying warm and fertile peridotite (Ballmer et al., 2007). Because SSC produces decompression melting in an elongated shape, it explains non-age-progressive volcanic chains that disagree with predictions of hot spot theory (Wilson, 1963).

The alternating slow and fast V_p anomalies in our model may be associated with SSC occurring at the sublithospheric thermal boundary layer of the old oceanic plates (Richter, 1973). Our model shows a slow- V_p anomaly subparallel to the plate motion in the East Mariana Basin (S1), which is in line with the general form of convective rolls aligned with the apparent plate motion direction (Davaille & Jaupart, 1994). Such an alignment trend is unclear for fast- and slow- V_p anomalies beneath the Pigafetta Basin (F1 and S2).

In the Pacific, previous studies have suggested a possible link between small-scale convection and gravity rolls (e.g., Eilon, Zhang, et al., 2022; Harmon et al., 2006, 2007, 2011), which are visible in satellite data (Haxby & Weissel, 1986). Additionally, a broadband Rayleigh-wave dispersion array analysis in the oldest Pacific seafloor indicates average 1-D V_s profile with significantly slow asthenosphere, providing evidence of reheating processes such as small-scale convection in the study region (Kawano, Isse, Takeo, et al., 2023). Our study region is situated in an area where the general trend of gravity lineations is in a northwestern orientation (Figure S19 in Supporting Information S1) and aligned with the absolute plate motion direction. In particular, negative gravity anomalies are present in close proximity to the slow-velocity anomalies (S1 and S2) in our study area (Figure 6). Our observations may indicate the existence of a more complex pattern of sublithospheric SSC, as suggested by Korenaga and Jordan (2004).

A numerical modeling study by Ballmer et al. (2009) suggested SSC activity below a relatively young (20–60 Myr) oceanic plate. The activity period of SSC is roughly consistent with the ages of seamounts in the western Pacific (e.g., formation of the MST at ~100 Ma on the 50–90 Myr old seafloor; Koppers et al., 2003). Therefore, the V_p anomalies observed below the oldest Pacific seafloor could be related to fossils of SSC, which were active ~100 Ma. It might be possible to maintain contrasts in temperature and volatile contents in the asthenosphere over a long time under the slow thermal diffusion state. However, the fossil SSC structure requires strong coupling between the lithosphere and asthenosphere to remain beneath the oldest Pacific region for a long time (~100 Myr).

On the other hand, the V_p anomalies can also be ascribed to SSC at present based on the numerical model of Likerman et al. (2021), which suggests that the SSC processes can provide a possible explanation for the Curie-point depth patterns observed in the old (>70–90 Myr old) lithosphere in the North Atlantic. In this case, other processes were required for the origin of the western Pacific seamounts. The MST and seamounts in the western Pacific may have formed because of the short-lived and discontinuous plume activity during the Cretaceous (Koppers et al., 2003).

Nevertheless, the spatially limited coverage of our observation (~1,000 km × 1,000 km) may not be able to fully determine the overall linear pattern of the SSC beneath the study area. Adam et al. (2021) suggested the existence of an SSC with a wavelength of ~1,000 km for the Pacific Plate based on the elongation of the lithospheric thickness, bathymetric lows, and geoid anomalies parallel to the direction of present-day Pacific Plate motion. This necessitates future ocean-bottom geophysical experiments on the oldest Pacific Plate.

5. Conclusions

Finite-frequency tomography with relative P -wave travel time residuals from 80 teleseismic earthquakes was conducted to obtain the upper mantle V_p structure beneath the oldest Pacific seafloor. This study used 1-year BBOBS data recorded from the Oldest-1 array experiment conducted from 2018 to 2019. The array covered the EMB in the southwest, the PB in the northeast, and the MST traversed the two basins in the northwest to southeast direction. Our final velocity model, assessed using a series of resolution tests, revealed two slow- V_p anomalies and one fast- V_p anomaly in the mantle below the basins and seamount trail. Two notable slow- V_p anomalies were below the MST and the oldest Pacific seafloor (>170 Ma) at depths of 95–305 km. The fast- V_p anomaly under the PB has a radius of ~200 km and a depth of 95–185 km. The observed slow anomalies are interpreted as being caused by a combination of relatively high temperature and partial melt, whereas the high-velocity region could be relatively dry, viscous, and rigid. Our model captures the dynamic nature of the evolution of the old Pacific Plate related to plume activity and (or) sublithospheric small-scale convection. Among the candidate scenarios considered, given the available geological/geophysical constraints, the most preferred scenario was that multiple plume activities produced the velocity anomaly as the plate moved across those hotspot regions. In this scenario, multiple plume activities may have resulted in the underplating of melt residue at the base of the lithosphere, causing the present-day fast seismic velocity structure. A more extensive study over a vast region of the oldest Pacific is required to better understand the relationship between plate dynamics and plume activities.

Data Availability Statement

BBOBS data acquired at the Oldest-1 experiment can be openly accessed from the Ocean Hemisphere Project Data Management Center (OHPDMC, 2023; <http://ohpdmc.eri.u-tokyo.ac.jp/dataset/campaign/obs/index.html>) in September 2023 after the moratorium period. Information of teleseismic events and relative travel time measurements obtained through the MCCC method (VanDecar & Crosson, 1990) are included in Tables S2–S4 and Figure S20 of Supporting Information S1. The analytical codes for tomographic imaging is available on Github (Hung, 2023). Most figures were created using PyGMT (v0.7.0) (Uieda et al., 2021). Perceptually uniform color map was generated by Crameri (2021) and is available at <https://www.fabiocrameri.ch/colourmaps/>. Movie S1 was created using MATLAB R2020a. The global models can be downloaded from the following sources: PAC-age (Isse, 2021), SPiRaL (Simmons et al., 2021b), SP12RTS (Koelemeijer et al., 2016b), HMSL (Houser et al., 2008a), and SPani (Tesoniero et al., 2015b).

Acknowledgments

The authors thank the captains, crew members, and scientists on board RV *Isabu* and RV *Onnuri* for their cooperation and logistical support. H. Kang, YH. Kim, and S.-M. Lee acknowledge funding (PE99656 and PE99796) from the Korea Institute of Ocean Science and Technology (KIOST) for the work. YH. Kim and H. Kang acknowledge funding from a National Research Foundation of Korea (NRF) grant by the Korean government (No. 2022R1A2C1003006 and 2022R1A5A1085103). This work was also supported by JSPS KAKENHI (Grant 18H03735). The authors thank HyeJeong Kim (Earthquake Research Institute; Seoul National University) for providing the synthetic waveforms and discussion on near-surface structures of the study region, Hwaju Lee (Seoul National University) for help with temperature estimation, and Hogyum Kim (Seoul National University) for discussions on the interpretation of our velocity model. We thank Editor and Associate Editor's support to this work and appreciate two anonymous reviewers for their thoughtful comments and constructive reviews.

References

- Abrams, L. J., Larson, R. L., Shipley, T. H., & Lancelot, Y. (1993). Cretaceous volcanic sequences and Jurassic oceanic crust in the East Mariana and Pigafetta basins of the western Pacific. *Washington DC American Geophysical Union Geophysical Monograph Series*, 77, 77–101. <https://doi.org/10.1029/GM077p0077>
- Adam, C., Vidal, V., Pandit, B., Davaille, A., & Kempton, P. D. (2021). Lithosphere destabilization and small-scale convection constrained from geophysical data and analogical models. *Geochemistry, Geophysics, Geosystems*, 22(3), e2020GC009462. <https://doi.org/10.1029/2020GC009462>
- Allen, R. M., Nolet, G., Morgan, W. J., Vogfjörð, K., Bergsson, B. H., Erlendsson, P., et al. (2002). Imaging the mantle beneath Iceland using integrated seismological techniques. *Journal of Geophysical Research*, 107(B12), ESE 3–1–ESE 3–16. <https://doi.org/10.1029/2001JB000595>
- Asimow, P. D., & Langmuir, A. C. (2003). The importance of water to oceanic mantle melting regimes. *Nature*, 421(6925), 815–820. <https://doi.org/10.1038/nature01429>
- Baba, K., Tada, N., Matsuno, T., Liang, P., Li, R., Zhang, L., et al. (2017). Electrical conductivity of old oceanic mantle in the northwestern Pacific I: 1-D profiles suggesting differences in thermal structure not predictable from a plate cooling model. *Earth, Planets and Space*, 69(1), 1–23. <https://doi.org/10.1186/s40623-017-0697-0>
- Babuška, V., & Plomerová, J. (2006). European mantle lithosphere assembled from rigid microplates with inherited seismic anisotropy. *Physics of the Earth and Planetary Interiors*, 158(2–4), 264–280. <https://doi.org/10.1016/j.pepi.2006.01.010>
- Babuška, V., Plomerová, J., & Šílený, J. (1984). Spatial variations of P residuals and deep structure of the European lithosphere. *Geophysical Journal International*, 79(1), 363–383. <https://doi.org/10.1111/j.1365-246X.1984.tb02863.x>
- Ballmer, M. D., Van Hunen, J., Ito, G., Tackley, P. J., & Bianco, T. A. (2007). Non-hotspot volcano chains originating from small-scale sublithospheric convection. *Geophysical Research Letters*, 34(23), L23310. <https://doi.org/10.1029/2007GL031636>
- Ballmer, M. D., Van Hunen, J., Ito, G., Bianco, T. A., & Tackley, P. J. (2009). Intraplate volcanism with complex age-distance patterns: A case for small-scale sublithospheric convection. *Geochemistry, Geophysics, Geosystems*, 10(6), Q06015. <https://doi.org/10.1029/2009GC002386>
- Barcheck, G., Abers, G. A., Adams, A. N., Bécél, A., Collins, J., Gaherty, J. B., et al. (2020). The Alaska amphibious community seismic experiment. *Seismological Society of America*, 91(6), 3054–3063. <https://doi.org/10.1785/0220200189>
- Barrauol, G., & Sigloch, K. (2013). Investigating La Réunion hot spot from crust to core. *Eos, Transactions American Geophysical Union*, 94(23), 205–207. <https://doi.org/10.1002/2013EO230002>
- Becker, T. W., Conrad, C. P., Schaeffer, A. J., & Lebedev, S. (2014). Origin of azimuthal seismic anisotropy in oceanic plates and mantle. *Earth and Planetary Science Letters*, 401, 236–250. <https://doi.org/10.1016/j.epsl.2014.06.014>
- Bie, L., Rietbrock, A., Hicks, S., Allen, R., Blundy, J., Clouard, V., et al. (2020). Along-arc heterogeneity in local seismicity across the Lesser Antilles subduction zone from a dense ocean-bottom seismometer network. *Seismological Research Letters*, 91(1), 237–247. <https://doi.org/10.1785/0220190147>
- Bird, P. (2003). An updated digital model of plate boundaries. *Geochemistry, Geophysics, Geosystems*, 4(3), 1027. <https://doi.org/10.1029/2001GC000252>
- Cammarano, F., Goes, S., Vacher, P., & Giardini, D. (2003). Inferring upper-mantle temperatures from seismic velocities. *Physics of the Earth and Planetary Interiors*, 138(3–4), 197–222. [https://doi.org/10.1016/S0031-9201\(03\)00156-0](https://doi.org/10.1016/S0031-9201(03)00156-0)
- Castillo, P. R., Pringle, M. S., & Carlson, R. W. (1994). East Mariana Basin tholeiites: Cretaceous intraplate basalts or rift basalts related to the Ontong Java plume? *Earth and Planetary Science Letters*, 123(1–3), 139–154. [https://doi.org/10.1016/0012-821X\(94\)90263-1](https://doi.org/10.1016/0012-821X(94)90263-1)
- Coffin, M. F., Duncan, R. A., Eldholm, O., Fitton, J. G., Frey, F. A., Larsen, H. C., et al. (2006). Large igneous provinces and scientific ocean drilling: Status quo and a look ahead. *Oceanography*, 19(4), 150–160. <https://doi.org/10.5670/oceanog.2006.13>
- Conrad, C. P., & Lithgow-Bertelloni, C. (2006). Influence of continental roots and asthenosphere on plate-mantle coupling. *Geophysical Research Letters*, 33(5), L05312. <https://doi.org/10.1029/2005GL025621>
- Crameri, F. (2021). Scientific colour maps (7.0.1) [Dataset]. Zenodo. <https://doi.org/10.5281/zenodo.5501399>
- Davaille, A., & Jaupart, C. (1994). Onset of thermal convection in fluids with temperature-dependent viscosity: Application to the oceanic mantle. *Journal of Geophysical Research*, 99(B10), 19853–19866. <https://doi.org/10.1029/94JB01405>
- Dziewonski, A. M., & Anderson, D. L. (1981). Preliminary reference Earth model. *Physics of the Earth and Planetary Interiors*, 25(4), 297–356. [https://doi.org/10.1016/0031-9201\(81\)90046-7](https://doi.org/10.1016/0031-9201(81)90046-7)
- Eberhart-Phillips, D., & Mark Henderson, C. (2004). Including anisotropy in 3-D velocity inversion and application to Marlborough, New Zealand. *Geophysical Journal International*, 156(2), 237–254. <https://doi.org/10.1111/j.1365-246X.2003.02044.x>
- Eilon, Z. C., Gaherty, J. B., Zhang, L., Russell, J., McPeak, S., Phillips, J., et al. (2022). The Pacific OBS research into convecting asthenosphere (ORCA) experiment. *Seismological Research Letters*, 93(1), 477–493. <https://doi.org/10.1785/02202010173>
- Eilon, Z. C., Zhang, L., Gaherty, J. B., Forsyth, D. W., & Russell, J. B. (2022). Sub-lithospheric small-scale convection tomographically imaged beneath the Pacific Plate. *Geophysical Research Letters*, 49(18), e2022GL100351. <https://doi.org/10.1029/2022GL100351>
- Eken, T., Plomerová, J., Vecsey, L., Babuška, V., Roberts, R., Shomali, H., & Bodvarsson, R. (2012). Effects of seismic anisotropy on P-velocity tomography of the Baltic Shield. *Geophysical Journal International*, 188(2), 600–612. <https://doi.org/10.1111/j.1365-246X.2011.05280.x>
- Ernst, R. E. (2014). *Large igneous provinces*. Cambridge University Press.

- Faul, U. H., & Jackson, I. (2005). The seismological signature of temperature and grain size variations in the upper mantle. *Earth and Planetary Science Letters*, 234(1–2), 119–134. <https://doi.org/10.1016/j.epsl.2005.02.008>
- Favier, N., Chevrot, S., & Komatitsch, D. (2004). Near-field influence on shear wave splitting and traveltime sensitivity kernels. *Geophysical Journal International*, 156(3), 467–482. <https://doi.org/10.1111/j.1365-246X.2004.02178.x>
- Fowler, C. M. R. (2004). *The solid earth: An introduction to global geophysics* (2nd ed.). Cambridge University Press.
- Fullea, J., Lebedev, S., Martinec, Z., & Celli, N. L. (2021). WINTERC-G: Mapping the upper mantle thermochemical heterogeneity from coupled geophysical–petrological inversion of seismic waveforms, heat flow, surface elevation and gravity satellite data. *Geophysical Journal International*, 226(1), 146–191. <https://doi.org/10.1093/gji/ggab094>
- Hable, S., Sigloch, K., Stutzmann, E., Kiselev, S., & Barruol, G. (2019). Tomography of crust and lithosphere in the western Indian Ocean from noise cross-correlations of land and ocean bottom seismometers. *Geophysical Journal International*, 219(2), 924–944. <https://doi.org/10.1093/gji/ggz333>
- Hammond, W. C., & Humphreys, E. D. (2000). Upper mantle seismic wave velocity: Effects of realistic partial melt geometries. *Journal of Geophysical Research*, 105(B5), 10975–10986. <https://doi.org/10.1029/2000JB900041>
- Harmon, N., Forsyth, D. W., Lamm, R., & Webb, S. C. (2007). P and S wave delays beneath intraplate volcanic ridges and gravity lineations near the East Pacific Rise. *Journal of Geophysical Research*, 112(B3), B03309. <https://doi.org/10.1029/2006JB004392>
- Harmon, N., Forsyth, D. W., Scheirer, D. S., & Duncan, R. A. (2006). Analysis of gravity and topography in the GLIMPSE study region: Isostatic compensation and uplift of the Sojourn and Hotu Matua Ridge systems. *Journal of Geophysical Research*, 111(B11), B11406. <https://doi.org/10.1029/2005JB004075>
- Harmon, N., Forsyth, D. W., Weeraratne, D. S., Yang, Y., & Webb, S. C. (2011). Mantle heterogeneity and off axis volcanism on young Pacific lithosphere. *Earth and Planetary Science Letters*, 311(3–4), 306–315. <https://doi.org/10.1016/j.epsl.2011.09.038>
- Haxby, W. F., & Weissel, J. K. (1986). Evidence for small-scale mantle convection from Seasat altimeter data. *Journal of Geophysical Research*, 91(B3), 3507–3520. <https://doi.org/10.1029/JB091iB03p03507>
- Hirschmann, M. M. (2000). Mantle solidus: Experimental constraints and the effects of peridotite composition. *Geochemistry, Geophysics, Geosystems*, 1(10). <https://doi.org/10.1029/2000GC000070>
- Houser, C., Masters, G., Shearer, P., & Laske, G. (2008a). HMSL [Model]. Retrieved from <https://members.elsi.jp/~chouser/models.html>
- Houser, C., Masters, G., Shearer, P., & Laske, G. (2008b). Shear and compressional velocity models of the mantle from cluster analysis of long-period waveforms. *Geophysical Journal International*, 174(1), 195–212. <https://doi.org/10.1111/j.1365-246X.2008.03763.x>
- Houtz, R. E., & Ludwig, W. J. (1979). Distribution of reverberant subbottom layers in the southwest Pacific basin. *Journal of Geophysical Research*, 84(B7), 3497–3504. <https://doi.org/10.1029/JB084iB07p03497>
- Hung, S.-H. (2023). BDFFT [Software]. Github. Retrieved from <https://github.com/shung302/BDFFT>
- Hung, S.-H., Chen, W. P., & Chiao, L. Y. (2011). A data-adaptive, multiscale approach of finite-frequency, traveltime tomography with special reference to P and S wave data from central Tibet. *Journal of Geophysical Research*, 116(B6), B06307. <https://doi.org/10.1029/2010JB008190>
- Hung, S.-H., Dahlen, F. A., & Nolet, G. (2000). Fréchet kernels for finite-frequency traveltimes—II. Examples. *Geophysical Journal International*, 141(1), 175–203. <https://doi.org/10.1046/j.1365-246X.2000.00072.x>
- Hung, S.-H., Shen, Y., & Chiao, L. Y. (2004). Imaging seismic velocity structure beneath the Iceland hot spot: A finite frequency approach. *Journal of Geophysical Research*, 109(B8). <https://doi.org/10.1029/2003JB002889>
- Isse, T. (2021). PAC-age model [Model]. *ResearchGate*. <https://doi.org/10.13140/RG.2.2.17421.05600>
- Isse, T., Kawakatsu, H., Yoshizawa, K., Takeo, A., Shiobara, H., Sugioka, H., et al. (2019). Surface wave tomography for the Pacific Ocean incorporating seafloor seismic observations and plate thermal evolution. *Earth and Planetary Science Letters*, 510, 116–130. <https://doi.org/10.1016/j.epsl.2018.12.033>
- Isse, T., Suetsugu, D., Ishikawa, A., Shiobara, H., Sugioka, H., Ito, A., et al. (2021). Seismic evidence for a thermochemical mantle plume underplating the lithosphere of the Ontong Java Plateau. *Communications Earth & Environment*, 2(1), 1–7. <https://doi.org/10.1038/s43247-021-00169-9>
- Ito, A., Shiobara, H., Miller, M., Sugioka, H., Ojeda, J., Tassara, C., et al. (2023). Long-term array observation by ocean bottom seismometers at the Chile Triple Junction. *Journal of South American Earth Sciences*, 124, 104285. <https://doi.org/10.1016/j.jsames.2023.104285>
- Jackson, M. G., Becker, T. W., & Steinberger, B. (2021). Spatial characteristics of recycled and primordial reservoirs in the deep mantle. *Geochemistry, Geophysics, Geosystems*, 22(3), e2020GC009525. <https://doi.org/10.1029/2020GC009525>
- Jackson, M. G., Hart, S. R., Konter, J. G., Koppers, A. A., Staudigel, H., Kurz, M. D., et al. (2010). Samoan hot spot track on a “hot spot highway”: Implications for mantle plumes and a deep Samoan mantle source. *Geochemistry, Geophysics, Geosystems*, 11(12), Q12009. <https://doi.org/10.1029/2010GC003232>
- Janiszewski, H. A., & Abers, G. A. (2015). Imaging the plate interface in the Cascadia seismogenic zone: New constraints from offshore receiver functions. *Seismological Research Letters*, 86(5), 1261–1269. <https://doi.org/10.1785/0220150104>
- Jordan, T. H. (1979). Mineralogies, densities and seismic velocities of garnet lherzolites and their geophysical implications, *The mantle sample: Inclusion in kimberlites and other volcanics* (Vol. 16, pp. 1–14). <https://doi.org/10.1029/SP016p0001>
- Karato, S.-I. (1995). Effects of water on seismic wave velocities in the upper mantle. *Proceedings of the Japan Academy, Series B*, 71(2), 61–66. <https://doi.org/10.2183/pjab.71.61>
- Karato, S.-I., & Jung, H. (1998). Water, partial melting and the origin of the seismic low velocity and high attenuation zone in the upper mantle. *Earth and Planetary Science Letters*, 157(3–4), 193–207. [https://doi.org/10.1016/S0012-821X\(98\)00034-X](https://doi.org/10.1016/S0012-821X(98)00034-X)
- Kawakatsu, H., & Utada, H. (2017). Seismic and electrical signatures of the lithosphere–asthenosphere system of the normal oceanic mantle. *Annual Review of Earth and Planetary Sciences*, 45(1), 139–167. <https://doi.org/10.1146/annurev-earth-063016-020319>
- Kawano, Y., Isse, T., Kawakatsu, H., Shiobara, H., Takeuchi, N., Sugioka, H., et al. (2023). Noise reduction from vertical-component seismograms recorded by broadband ocean-bottom seismometers deployed at the Western Pacific. *Bulletin of the Seismological Society of America*, 113(4), 1759–1771. <https://doi.org/10.1785/0120220256>
- Kawano, Y., Isse, T., Takeo, A., Kawakatsu, H., Morishige, M., Shiobara, H., et al. (2023). Seismic structure of the lithosphere–asthenosphere system beneath the oldest seafloor revealed by Rayleigh-wave dispersion analysis. *Journal of Geophysical Research: Solid Earth*, 128(6), e2023JB026529. <https://doi.org/10.1029/2023JB026529>
- Kim, H., Baba, K., Utada, H., Shimizu, H., Lee, S. M., Kawakatsu, H., & Kim, Y. (2020). Preliminary 1-D electrical conductivity structure of oldest oceanic mantle from magnetotelluric observation, Pacific Array project. In *AGU Fall Meeting Abstracts* (Vol. 2020, D1012–0007).
- Kim, H., Kawakatsu, H., Akuhara, T., Shinohara, M., Shiobara, H., Sugioka, H., & Takagi, R. (2021). Receiver function imaging of the amphibious NE Japan subduction zone—Effects of low-velocity sediment layer. *Journal of Geophysical Research: Solid Earth*, 126(9), e2021JB021918. <https://doi.org/10.1029/2021JB021918>

- Kim, T.-S., Park, J.-H., Ko, J.-W., Oh, S.-Y., Witek, M., Chang, S.-J., et al. (2023). Characteristics of background noise in the oldest-1 array deployed on the oldest part of the Pacific Plate. *Bulletin of the Seismological Society of America*, 113(4), 1772–1793. <https://doi.org/10.1785/0120220215>
- Koelemeijer, P., Ritsema, J., Deuss, A., & Van Heijst, H. J. (2016a). SP12RTS: A degree-12 model of shear-and compressional-wave velocity for Earth's mantle. *Geophysical Journal International*, 204(2), 1024–1039. <https://doi.org/10.1093/gji/ggv481>
- Koelemeijer, P., Ritsema, J., Deuss, A., & Van Heijst, H. J. (2016b). SP12RTS [Model]. Retrieved from https://www.earth.ox.ac.uk/~univ4152/downloads_sp12rts.html
- Koppers, A. A., Staudigel, H., Pringle, M. S., & Wijbrans, J. R. (2003). Short-lived and discontinuous intraplate volcanism in the South Pacific: Hot spots or extensional volcanism? *Geochemistry, Geophysics, Geosystems*, 4(10). <https://doi.org/10.1029/2003GC000533>
- Korenaga, J., & Jordan, T. H. (2004). Physics of multiscale convection in Earth's mantle: Evolution of sublithospheric convection. *Journal of Geophysical Research*, 109(B1), 2333. <https://doi.org/10.1029/2003JB002464>
- Laske, G., Masters, G., Ma, Z., & Pasyanos, M. (2013). Update on CRUST1. 0—A 1-degree global model of Earth's crust. In *Geophysical Research Abstracts* (Vol. 15, p. 2658). EGU General Assembly.
- Le, B. M., Yang, T., & Phipps Morgan, J. (2022). Seismic constraints on crustal and uppermost mantle structure beneath the Hawaiian swell: Implications for plume-lithosphere interactions. *Journal of Geophysical Research: Solid Earth*, 127(11), e2021JB023822. <https://doi.org/10.1029/2021JB023822>
- Lee, C.-T. A. (2003). Compositional variation of density and seismic velocities in natural peridotites at STP conditions: Implications for seismic imaging of compositional heterogeneities in the upper mantle. *Journal of Geophysical Research*, 108(B9), 2441. <https://doi.org/10.1029/2003JB002413>
- Lee, H., Bezada, M. J., & Faccenda, M. (2021). Can sub-slab low-velocity anomalies be an artifact caused by anisotropy? A case study from the Alboran slab area in the western Mediterranean. *Tectonophysics*, 819, 229080. <https://doi.org/10.1016/j.tecto.2021.229080>
- Likerman, J., Zlotnik, S., & Li, C. F. (2021). The effects of small-scale convection in the shallow lithosphere of the North Atlantic. *Geophysical Journal International*, 227(3), 1512–1522. <https://doi.org/10.1093/gji/ggab286>
- Lin, P.-Y. P., Gaherty, J. B., Jin, G., Collins, J. A., Lizarralde, D., Evans, R. L., & Hirth, G. (2016). High-resolution seismic constraints on flow dynamics in the oceanic asthenosphere. *Nature*, 535(7613), 538–541. <https://doi.org/10.1038/nature18012>
- Ma, Z., Dalton, C. A., Russell, J. B., Gaherty, J. B., Hirth, G., & Forsyth, D. W. (2020). Shear attenuation and anelastic mechanisms in the central Pacific upper mantle. *Earth and Planetary Science Letters*, 536, 116148. <https://doi.org/10.1016/j.epsl.2020.116148>
- Mahoney, J. J. (1987). An isotopic survey of Pacific oceanic plateaus: Implications for their nature and origin. *Seamounts, Islands, and Atolls*, 43, 207–220. <https://doi.org/10.1029/GM043p0207>
- McKenzie, D. (1985). The extraction of magma from the crust and mantle. *Earth and Planetary Science Letters*, 74(1), 81–91. [https://doi.org/10.1016/0012-821X\(85\)90168-2](https://doi.org/10.1016/0012-821X(85)90168-2)
- McKenzie, D., Jackson, J., & Priestley, K. (2005). Thermal structure of oceanic and continental lithosphere. *Earth and Planetary Science Letters*, 233(3–4), 337–349. <https://doi.org/10.1016/j.epsl.2005.02.005>
- McNutt, M. K. (1998). Superswells. *Reviews of Geophysics*, 36(2), 211–244. <https://doi.org/10.1029/98RG00255>
- McNutt, M. K., & Fischer, K. M. (1987). The South Pacific superswell, seamounts, islands, and atolls (Vol. 43, pp. 25–34). <https://doi.org/10.1029/GM043p0025>
- Müller, R. D., Sdrolias, M., Gaina, C., & Roest, W. R. (2008). Age, spreading rates, and spreading asymmetry of the world's ocean crust. *Geochemistry, Geophysics, Geosystems*, 9(4), Q04006. <https://doi.org/10.1029/2007GC001743>
- Nakanishi, M., Tamaki, K., & Kobayashi, K. (1992). Magnetic anomaly lineations from late Jurassic to early cretaceous in the west-central Pacific Ocean. *Geophysical Journal International*, 109(3), 701–719. <https://doi.org/10.1111/j.1365-246X.1992.tb00126.x>
- OHPDMC. (2023). Oldest-1 project [Dataset]. OHPDMC. Retrieved from <http://ohpdmc.eri.u-tokyo.ac.jp/dataset/campaign/obs/index.html>
- Parsons, B., & Sclater, J. G. (1977). An analysis of the variation of ocean floor bathymetry and heat flow with age. *Journal of Geophysical Research*, 82(5), 803–827. <https://doi.org/10.1029/JB082i005p00803>
- Pasyanos, M. E., Masters, T. G., Laske, G., & Ma, Z. (2014). LITHO1. 0: An updated crust and lithospheric model of the Earth. *Journal of Geophysical Research: Solid Earth*, 119(3), 2153–2173. <https://doi.org/10.1002/2013JB010626>
- Pavoni, N. (2003). Pacific microplate and the Pangea supercontinent in the Early to Middle Jurassic: Comment and Reply: COMMENT. *Geology*, 31(1), e1–e2. <https://doi.org/10.1130/0091-7613-31.1.e1>
- Peterson, J. R. (1993). *Observations and modeling of seismic background noise*. US Geological Survey. <https://doi.org/10.3133/ofr93322>
- Phipps Morgan, J., Morgan, W. J., & Price, E. (1995). Hotspot melting generates both hotspot volcanism and a hotspot swell? *Journal of Geophysical Research*, 100(B5), 8045–8062. <https://doi.org/10.1029/94JB02887>
- Phipps Morgan, J., Morgan, W. J., Zhang, Y. S., & Smith, W. H. (1995). Observational hints for a plume-fed, suboceanic asthenosphere and its role in mantle convection. *Journal of Geophysical Research*, 100(B7), 12753–12767. <https://doi.org/10.1029/95JB00041>
- Priestley, K., McKenzie, D., & Ho, T. (2018). A lithosphere–asthenosphere boundary—A global model derived from multimode surface-wave tomography and petrology. *Lithospheric Discontinuities*, 111–123. <https://doi.org/10.1002/9781119249740.ch6>
- Ricard, Y., Doglioni, C., & Sabadini, R. (1991). Differential rotation between lithosphere and mantle: A consequence of lateral mantle viscosity variations. *Journal of Geophysical Research*, 96(B5), 8407–8415. <https://doi.org/10.1029/91JB00204>
- Richter, F. M. (1973). Convection and the large-scale circulation of the mantle. *Journal of Geophysical Research*, 78(35), 8735–8745. <https://doi.org/10.1029/JB078i035p08735>
- Rost, S., & Williams, Q. (2003). Seismic detection of sublithospheric plume head residue beneath the Pitcairn hot-spot chain. *Earth and Planetary Science Letters*, 209(1–2), 71–83. [https://doi.org/10.1016/S0012-821X\(03\)00075-X](https://doi.org/10.1016/S0012-821X(03)00075-X)
- Russell, J. B., Gaherty, J. B., Lin, P.-Y. P., Lizarralde, D., Collins, J. A., Hirth, G., & Evans, R. L. (2019). High-resolution constraints on Pacific upper mantle petrofabric inferred from surface-wave anisotropy. *Journal of Geophysical Research: Solid Earth*, 124(1), 631–657. <https://doi.org/10.1029/2018JB016598>
- Schlömer, A., Geissler, W. H., Jokat, W., & Jegen, M. (2017). Hunting for the Tristan mantle plume—An upper mantle tomography around the volcanic island of Tristan da Cunha. *Earth and Planetary Science Letters*, 462, 122–131. <https://doi.org/10.1016/j.epsl.2016.12.028>
- Seno, T., & Yamanaka, Y. (1996). Double seismic zones, compressional deep trench-outer rise events, and superplumes. *Washington DC American Geophysical Union Geophysical Monograph Series*, 96, 347–355. <https://doi.org/10.1029/GM096p0347>
- Shintaku, N., Forsyth, D. W., Hajewski, C. J., & Weeraratne, D. S. (2014). Pn anisotropy in Mesozoic western Pacific lithosphere. *Journal of Geophysical Research: Solid Earth*, 119(4), 3050–3063. <https://doi.org/10.1002/2013JB010534>
- Shiobara, H., Ito, A., Sugioka, H., Shinohara, M., & Sato, T. (2021). Tilt observations at the seafloor by mobile ocean bottom seismometers. *Frontiers in Earth Science*, 749, 599810. <https://doi.org/10.3389/feart.2020.599810>

- Simmons, N. A., Myers, S. C., Morency, C., Chiang, A., & Knapp, D. R. (2021a). SPiRaL: A multiresolution global tomography model of seismic wave speeds and radial anisotropy variations in the crust and mantle. *Geophysical Journal International*, 227(2), 1366–1391. <https://doi.org/10.1093/gji/ggab277>
- Simmons, N. A., Myers, S. C., Morency, C., Chiang, A., & Knapp, D. R. (2021b). SPiRaL [Model]. <https://doi.org/10.17611/dp/emc.2021.spiral.1>
- Smith, W. H., Staudigel, H., Watts, A. B., & Pringle, M. S. (1989). The Magellan Seamounts: Early Cretaceous record of the South Pacific isotopic and thermal anomaly. *Journal of Geophysical Research*, 94(B8), 10501–10523. <https://doi.org/10.1029/JB094iB08p10501>
- Stähler, S. C., Sigloch, K., Hosseini, K., Crawford, W. C., Barruol, G., Schmidt-Aursch, M. C., et al. (2016). Performance report of the RHUM-RUM ocean bottom seismometer network around La Réunion, western Indian Ocean. *Advances in Geosciences*, 41, 43–63. <https://doi.org/10.5194/adgeo-41-43-2016>
- Sumy, D. F., Lodewyk, J. A., Woodward, R. L., & Evers, B. (2015). Ocean-bottom seismograph performance during the Cascadia initiative. *Seismological Research Letters*, 86(5), 1238–1246. <https://doi.org/10.1785/0220150110>
- Takeo, A., Forsyth, D. W., Weeraratne, D. S., & Nishida, K. (2014). Estimation of azimuthal anisotropy in the NW Pacific from seismic ambient noise in seafloor records. *Geophysical Journal International*, 199(1), 11–22. <https://doi.org/10.1093/gji/ggu240>
- Takeo, A., Kawakatsu, H., Isse, T., Nishida, K., Shiobara, H., Sugioka, H., et al. (2018). In situ characterization of the lithosphere-asthenosphere system beneath NW Pacific Ocean via broadband dispersion survey with two OBS arrays. *Geochemistry, Geophysics, Geosystems*, 19(9), 3529–3539. <https://doi.org/10.1029/2018GC007588>
- Takeo, A., Kawakatsu, H., Isse, T., Nishida, K., Sugioka, H., Ito, A., et al. (2016). Seismic azimuthal anisotropy in the oceanic lithosphere and asthenosphere from broadband surface wave analysis of OBS array records at 60 Ma seafloor. *Journal of Geophysical Research: Solid Earth*, 121(3), 1927–1947. <https://doi.org/10.1002/2015JB012429>
- Takeo, A., Nishida, K., Isse, T., Kawakatsu, H., Shiobara, H., Sugioka, H., & Kanazawa, T. (2013). Radially anisotropic structure beneath the Shikoku Basin from broadband surface wave analysis of ocean bottom seismometer records. *Journal of Geophysical Research: Solid Earth*, 118(6), 2878–2892. <https://doi.org/10.1002/jgrb.50219>
- Takeuchi, N., Kawakatsu, H., Shiobara, H., Isse, T., Sugioka, H., Ito, A., & Utada, H. (2017). Determination of intrinsic attenuation in the oceanic lithosphere-asthenosphere system. *Science*, 358(6370), 1593–1596. <https://doi.org/10.1126/science.aao3508>
- Takeuchi, N., Kawakatsu, H., Shiobara, H., Isse, T., Sugioka, H., Ito, A., & Utada, H. (2020). Inversion of longer-period OBS waveforms for P structures in the oceanic lithosphere and asthenosphere. *Journal of Geophysical Research: Solid Earth*, 125(7), e2019JB018810. <https://doi.org/10.1029/2019JB018810>
- Tesoniero, A., Auer, L., Boschi, L., & Cammarano, F. (2015a). Hydration of marginal basins and compositional variations within the continental lithospheric mantle inferred from a new global model of shear and compressional velocity. *Journal of Geophysical Research: Solid Earth*, 120(11), 7789–7813. <https://doi.org/10.1002/2015JB012026>
- Tesoniero, A., Auer, L., Boschi, L., & Cammarano, F. (2015b). SPani [Model]. <https://doi.org/10.17611/DP/EMCSPANI>
- Tharimena, S., Rychert, C. A., & Harmon, N. (2016). Seismic imaging of a mid-lithospheric discontinuity beneath Ontong Java Plateau. *Earth and Planetary Science Letters*, 450, 62–70. <https://doi.org/10.1016/j.epsl.2016.06.026>
- Tian, Y., Hung, S.-H., Nolet, G., Montelli, R., & Dahlen, F. A. (2007). Dynamic ray tracing and traveltimes corrections for global seismic tomography. *Journal of Computational Physics*, 226(1), 672–687. <https://doi.org/10.1016/j.jcp.2007.04.025>
- Tsekhmistrov, M., Sigloch, K., Hosseini, K., & Barruol, G. (2021). A tree of Indo-African mantle plumes imaged by seismic tomography. *Nature Geoscience*, 14(8), 612–619. <https://doi.org/10.1038/s41561-021-00762-9>
- Uieda, L., Tian, D., Leong, W. J., Toney, L., Schlitzer, W., Grund, M., et al. (2021). PyGMT: A Python interface for the generic mapping tools [Software]. Zenodo. <https://doi.org/10.5281/ZENODO.4522136>
- VanDecar, J., & Crosson, R. (1990). Determination of teleseismic relative phase arrival times using multi-channel cross-correlation and least squares. *Bulletin of the Seismological Society of America*, 80, 150–169. <https://doi.org/10.1785/BSSA0800010150>
- Wei, X., Zhang, Y., Shi, X. F., Castillo, P. R., Xu, Y. G., Yan, Q. S., & Liu, J. H. (2022). Co-occurrence of HIMU and EM1 components in a single Magellan Seamount: Implications for the formation of West Pacific seamount province. *Journal of Petrology*, 63(4), egac022. <https://doi.org/10.1093/petrology/egac022>
- Wessel, P., & Kroenke, L. W. (2008). Pacific absolute plate motion since 145 Ma: An assessment of the fixed hot spot hypothesis. *Journal of Geophysical Research*, 113(B6), B06101. <https://doi.org/10.1029/2007JB005499>
- Wilson, J. T. (1963). A possible origin of the Hawaiian Islands. *Canadian Journal of Physics*, 41(6), 863–870. <https://doi.org/10.1139/p63-094>
- Winterer, E. L., Natland, J. H., Van Waasbergen, R. J., Duncan, R. A., McNutt, M. K., Wolfe, C. J., et al. (1993). Cretaceous guyots in the north-west Pacific: An overview of their geology and geophysics. *The Mesozoic Pacific: Geology, Tectonics, and Volcanism*, 77, 307–334.
- Wolfe, C. J., & McNutt, M. K. (1991). Compensation of cretaceous seamounts of the Darwin Rise, northwest Pacific Ocean. *Journal of Geophysical Research*, 96(B2), 2363–2374. <https://doi.org/10.1029/90JB01893>
- Yamamoto, M., & Phipps Morgan, J. (2009). North Arch volcanic fields near Hawaii are evidence favouring the restite-root hypothesis for the origin of hotspot swells. *Terra Nova*, 21(6), 452–466. <https://doi.org/10.1111/j.1365-3121.2009.00902.x>
- Yang, H.-Y., & Hung, S.-H. (2005). Validation of ray and wave theoretical travel times in heterogeneous random media. *Geophysical Research Letters*, 32(20), L20302. <https://doi.org/10.1029/2005GL023501>

References From the Supporting Information

- Sandwell, D. T., Müller, R. D., Smith, W. H., Garcia, E., & Francis, R. (2014). New global marine gravity model from CryoSat-2 and Jason-1 reveals buried tectonic structure. *Science*, 346(6205), 65–67. <https://doi.org/10.1126/science.1258213>